Simulating Magnetohydrodynamical Flow with Constrained Transport and Adaptive Mesh Refinement; Algorithms & Tests of the AstroBEAR Code

Andrew J. Cunningham[1], Adam Frank[1], Peggy Varnière[1,2], Sorin Mitran[3], Thomas W. Jones[4]

ajc4@pas.rochester.edu

arXiv:0710.0424v4 [astro-ph] 19 Mar 2009

ABSTRACT

A description is given of the algorithms implemented in the AstroBEAR adaptive mesh refinement code for ideal magnetohydrodynamics. The code provides several high resolution, shock capturing schemes which are constructed to maintain conserved quantities of the flow in a finite volume sense. Divergence free magnetic field topologies are maintained to machine precision by collating the components of the magnetic field on a cell-interface staggered grid and utilizing the constrained transport approach for integrating the induction equations. The maintenance of magnetic field topologies on adaptive grids is achieved using prolongation and restriction operators which preserve the divergence and curl of the magnetic field across co-located grids of different resolution. The robustness and correctness of the code is demonstrated by comparing the numerical solution of various tests with analytical solutions or previously published numerical solutions obtained by other codes.

Subject headings: MHD, methods: numerical

---

[1]Department of Physics and Astronomy, University of Rochester, Rochester, NY 14054

[2]LAOG, Universit J. Fourier UMR5571, France

[3]University of North Carolina, Department of Mathematics, Chapel Hill, NC 27599

[4]Department of Astronomy, University of Minnesota, 116 Church Street SE, Minneapolis, MN 55455

1. Introduction

The development of efficient and accurate numerical algorithms for astrophysical flow has become of great interest to the astrophysical community. Variable resolution approaches have provided an avenue for efficient simulation of hydrodynamical flow including multi-physical effects which involve substantial variation in length scale. Adaptive Mesh Refinement (AMR) has been recognized as one of the most versatile and efficient approaches to enable the simulation of multi-scale phenomena for which fixed-resolution simulation is either impractical or impossible. AMR discretizations employ a hierarchy of grids at different levels. High resolution is applied only to those regions of the flow which would otherwise be subject to unacceptably large truncation error. The utility of the AMR approach is underscored by the extensive list of codes that are targeted toward astrophysical research which utilize AMR. The list includes AstroBEAR, Enzo (O'Shea et al. 2004), Flash (Fryxell et al. 2000), Orion (Truelove et al. 1998; Klein 1999; Crockett et al. 2005), Nirvana (Ziegler 2005a), Ramses (Fromang et al. 2006), RIEMANN (Balsara 2001) and AMRVAC (Keppens et al. 2003) and the list of codes for which the development AMR capability is in progress including Athena (Gardiner & Stone 2005) and Pluto (Mignone et al. 2007).

The simulation of magnetized flow is of particular interest to astrophysical researchers owing to the utility of numerical magnetohydrodynamics (MHD) in modeling a wide range of astrophysical phenomena. The leading line of recent research in this area has focused on the application of higher order Godunov methods to numerical MHD (Ryu & Jones 1995; Balsara 1998). The conservative formulation and proper upwinding employed by these methods enable accurate simulation of strongly supersonic flow. Because of this unique capability, such methods are often referred to "high resolution shock capturing" (HRSC) methods.

While HRSC methods have long been recognized as the defacto standard for the simulation of supersonic hydrodynamical phenomena, their popularity among researchers interested in magnetized flow has been slowed because standard HRSC approaches to MHD fail to maintain the solenoidality constraint on the magnetic field ($\nabla \cdot \mathbf{B} = 0$). If not corrected, local divergences in the magnetic field arising from this short coming usually grow rapidly, causing anomalous magnetic forces and unphysical plasma transport which eventually destroys the correct dynamics of the flow (Brackbill & Barnes 1980). Early practitioners of numerical MHD therefore relied heavily on finite difference methods as employed by codes such as Zeus Stone & Norman (1992) which maintain the solenoidality constraint exactly despite their inferior shock capturing ability (Falle 2002). Later works focused on improved HRSC which either eliminate the development of divergences in the magnetic field, or mitigate the effect of local divergence errors on the dynamics of the flow. In one such approach, a projection operator is devised, usually by solving a Poisson equation, which removes numerical

divergences from the grid after each time-step (Balsara 1998; Jiang & Wu 1999; Kim et al. 1999; Zachary et al. 1994; Ryu et al. 1995). The primary limitation of this approach is that non-trivial boundary value problems become indeterminate (Ryu et al. 1998). In the second so called "8-wave" approach first explored by Powell et al. (1999), alternative formulations of the MHD equations are constructed to prevent the local build up of magnetic divergence by advecting monopoles to other regions of the grid where they are of less consequence to the dynamics of the flow. The work of Dedner et al. (2002) augments this approach by adding source terms to the system which act to counter the effect of local divergence in the magnetic field on the dynamics of the flow. A third approach known as constrained transport utilizes a multidimensional, divergence-preserving update procedure for the magnetic field components which are collated on a staggered grid centered on the computational volume interfaces. (Evans & Hawley 1988; Ryu et al. 1998; Balsara & Spicer 1999; Dai & Woodward 1998; Londrillo & Del Zanna 2000; Ziegler 2005b). This approach has been shown to provide the most accurate results in the tests of Tóth (2000) and Balsara & Kim (2004).

The combination of AMR spatial discretizations with HRSC would seem a natural choice in order to satisfy the desire for a high accurate, computationally efficient and versatile strategy for the simulation of magnetized plasma flow. The implementation of the aforementioned adaptations to HRSC methods for MHD in an AMR framework however, poses several challenges. Divergence cleaning schemes utilizing a Poisson projection operator are ill-suited for AMR applications owing to difficulty in handling the projection step along internal boundaries on a patchwork of grids at different resolutions. Powell et al. (1999) found that the application of their 8-wave method on an AMR grid hierarchy, local divergence errors on one level of the AMR hierarchy caused local divergence of comparable magnitude on all levels. The main drawback of this method in an AMR context is that the unphysical effects of local divergences in the magnetic field are not diminished by the application of additional refinement. Crockett et al. (2005), however, have constructed an approach suitable for AMR applications which combines an approximate projection operator with the divergence advection and dampening the effects of local divergence of Powell et al. (1999) and Dedner et al. (2002).

Retaining the divergence-free property of the solution obtained through the application of the constrained transport approach on hierarchical grids requires application of a divergence-preserving prolongation operator which interpolates the magnetic field from a coarse mesh a fine mesh, a divergence-preserving restriction operator which maps the fine mesh magnetic field onto a coarser mesh and furthermore requires that the evolution of the magnetic field be consistent between collocated meshes of different resolution. Two approaches to these challenges have emerged. Balsara (2001) has generalized the divergence free reconstruction procedure of Balsara & Spicer (1999) to devise a prolongation operator

based on a piece-wise quadratic interpolation procedure that is divergence preserving in the RIEMANN MHD code. Li & Li (2004) present an adaptation of Balsara's procedure that simplifies its implementation for problems involving arbitrary refinement ratios. Tóth & Roe (2002) have devised a prolongation operator by solving an algebraic system which enforces the maintenance of the volume average curl and divergence between grids of different resolution in the AMR hierarchy.

In this paper we provide a concise description of the algorithms and tests of the AstroBEAR HRSC AMR MHD code. AstroBEAR is comprised of several numerical solvers, integration schemes, and radiative cooling modules for astrophysical fluids. The code's AMR capability is derived from the AMR engine of the BEARCLAW boundary embedded adaptive mesh refinement package for conservation laws. This code utilizes the constrained transport approach to adapting HRSC methods to the MHD system of equations. To our knowledge, AstroBEAR is the first AMR code to utilize the prolongation operator of Tóth & Roe (2002) to maintain the $\nabla \cdot \mathbf{B} = 0$ constraint. By combining multi-physics capabilities relevant to simulation astrophysical plasma flow, AMR, and a wide selection of HRSC integration procedures, AstroBEAR will serve as a valuable research tool. The authors intend that this paper will serve as a reference for future works that apply the code and provide a concise recipe for robust, reliable and accurate HRSC solution strategies for MHD on AMR grid hierarchies. In §2 we describe the several HRSC schemes and divergence preservation strategies implemented in the code. In §3 we provide an overview of the AMR algorithm, highlighting the stages which require special treatment of the magnetic field. In §4 we provide a concise description of the prolongation, restriction and coarse to fine refluxing procedures required to preserve the divergence and consistency of the magnetic field across an AMR hierarchy of grids. In §5 we comment on the results of several test and example problems with particular emphasis on the relative strengths and weaknesses of the various HRSC schemes implemented in the code. In §6 we provide a synopsis and discussion of the main results of the paper.

2. Numerical Method

AstroBEAR provides an adaptive mesh refinement framework for the integration of conservation laws of the form,

$$\frac{\partial}{\partial t}\mathbf{Q} + \frac{\partial}{\partial x}\mathbf{F}_x(\mathbf{Q}) + \frac{\partial}{\partial y}\mathbf{F}_y(\mathbf{Q}) + \frac{\partial}{\partial z}\mathbf{F}_z(\mathbf{Q}) = \mathbf{S}(\mathbf{Q}). \tag{1}$$

In this work we focus on the equations of ideal MHD which are written in the conservative form as:

$$\frac{\partial}{\partial t}\begin{bmatrix} \rho \\ \rho v_x \\ \rho v_y \\ \rho v_z \\ \mathcal{E} \\ B_x \\ B_y \\ B_z \end{bmatrix} + \frac{\partial}{\partial x}\begin{bmatrix} \rho v_x \\ \rho v_x^2 + P + B^2/2 - B_x^2 \\ \rho v_y v_x - B_x B_y \\ \rho v_z v_x - B_x B_z \\ (\mathcal{E} + P + \mathbf{B}^2/2)v_x - B_x(\mathbf{B} \cdot \mathbf{v}) \\ 0 \\ -E_z \\ E_y \end{bmatrix} +$$

$$\frac{\partial}{\partial y}\begin{bmatrix} \rho v_y \\ \rho v_x v_y - B_y B_x \\ \rho v_y^2 + P + B^2/2 - B_y^2 \\ \rho v_z v_y - B_y B_z \\ (\mathcal{E} + P + \mathbf{B}^2/2)v_y - B_y(\mathbf{B} \cdot \mathbf{v}) \\ E_z \\ 0 \\ -E_x \end{bmatrix} + \frac{\partial}{\partial z}\begin{bmatrix} \rho v_z \\ \rho v_x v_z - B_z B_x \\ \rho v_y v_z - B_z B_y \\ \rho v_z^2 + P + B^2/2 - B_z^2 \\ (\mathcal{E} + P + \mathbf{B}^2/2)v_z - B_z(\mathbf{B} \cdot \mathbf{v}) \\ -E_y \\ E_x \\ 0 \end{bmatrix} = \mathbf{S} \quad (2)$$

with gas density ρ, velocity $\mathbf{v}$, total volumetric energy density $\mathcal{E}$, thermal pressure P, magnetic field $\mathbf{B}$, and electric field $\mathbf{E}$. In the proceeding system of equations, we have chosen units for the electric and magnetic field in the plasma so that factors of 4π do not appear in the equations. The last three equations in the system follow from Faraday's law,

$$\frac{\partial}{\partial t}\mathbf{B} + \nabla \times \mathbf{E} = 0, \quad (3)$$

implicit to which is the constraint that initially solenoidal magnetic field topologies remain solenoidal,

$$\nabla \cdot \mathbf{B} = 0.$$

The equations are brought to a closed form via Ohm's law for a perfectly conducting medium,

$$\mathbf{E} = -\mathbf{v} \times \mathbf{B} \quad (4)$$

and the polytropic equation of state for an ideal gas,

$$P = (\gamma - 1)(\mathcal{E} - \rho\mathbf{v}^2/2 - \mathbf{B}^2/2). \quad (5)$$

In the remainder of this section, we describe the details of the shock capturing numerical schemes available in our code to integrate the solution to equations of the form of equation

1 and modifications thereof which ensure the solenoidal constraint on the magnetic field. The purpose of this description is to provide a concise and complete illustration of the steps necessary to build the code. The details of any of the particular solution strategies may be obtained by consulting the original work credited for the particular strategy. For a more pedagogically oriented review of high resolution shock capturing schemes, we refer the reader to the excellent books of Leveque (2002) and Toro (1999). In the remainder of this section, we consider only the solution method for the homogeneous part of the conservation law with $\mathbf{S} = 0$. The effect of non-zero source terms which may be used to include additional physics are handled using the operator splitting technique described in §2.1 of Cunningham et al. (2005). The micro-physical source terms included in the code to model the effects of radiative cooling, and time dependent, non-equilibrium ionization and H_2 chemistry are cataloged in the appendix to Cunningham et al. (2005). In appendix A we catalog the MHD source terms and modifications to the numerical scheme that are employed in applications involving cylindrical axisymmetric flow. We adopt the notation that superscripts denote time, the first subscript denotes the direction of vector components, and the last three subscripts denote the spatial location on the computational grid. The superscript is omitted from temporally varying quantities which are to be evaluated at time t. Equations which demonstrate operations that take the same form in each of the x, y, and z directions are written only for the x-direction sweep. In these cases, the y sweep can can be recovered by replacing $y \rightarrow x$ and $j \rightarrow i$ and the z sweep can can be retrieved by replacing $z \rightarrow x$ and $k \rightarrow i$.

Numerical integration of the system of conservation laws is achieved using the finite volume method. The basis of the finite volume quadrature can be realized by discretizing the integral form of equation 1, yielding the following unsplit procedure for advancing the conserved field forward in time by an increment Δt:

$$
\begin{aligned}
\mathbf{Q}_{i,j,k}^{t+\Delta t} &= \mathbf{Q}_{i,j,k}^{t} + \frac{\Delta t}{\Delta x}\left(\tilde{\mathbf{F}}_{x,i-1/2,j,k}^{n} - \tilde{\mathbf{F}}_{x,i+1/2,j,k}^{n}\right) + \\
&\quad \frac{\Delta t}{\Delta y}\left(\tilde{\mathbf{F}}_{y,i,j-1/2,k}^{n} - \tilde{\mathbf{F}}_{y,i,j+1/2,k}^{n}\right) + \frac{\Delta t}{\Delta z}\left(\tilde{\mathbf{F}}_{z,i,j,k-1/2}^{n} - \tilde{\mathbf{F}}_{z,i,j,k+1/2}^{n}\right).
\end{aligned}
\tag{6}
$$

where $\tilde{\mathbf{F}}_x^n$, $\tilde{\mathbf{F}}_x^n$, and $\tilde{\mathbf{F}}_x^n$ are suitably accurate numerical approximations to the inter-cell flux, spatially averaged over the inter-cell area and temporally averaged from t to $t+\Delta t$. Construction of higher order schemes in more than one dimension can, in some cases, be simplified by utilizing a direction-split approach

$$
\begin{aligned}
\mathbf{Q}_{i,j,k}^{(0)} &= \mathbf{Q}_{i,j,k}^{t} \\
\mathbf{Q}_{i,j,k}^{(1)} &= \mathbf{Q}_{i,j,k}^{(0)} + \frac{\Delta t}{\Delta x_1}\left(\tilde{\mathbf{F}}_{x1,i-1/2,j,k}^{n}(\mathbf{Q}_{i,j,k}^{(0)}) - \tilde{\mathbf{F}}_{x1,i+1/2,j,k}^{n}(\mathbf{Q}_{i,j,k}^{(0)})\right) \\
\mathbf{Q}_{i,j,k}^{(2)} &= \mathbf{Q}_{i,j,k}^{(1)} + \frac{\Delta t}{\Delta x_2}\left(\tilde{\mathbf{F}}_{x2,i-1/2,j,k}^{n}(\mathbf{Q}_{i,j,k}^{(1)}) - \tilde{\mathbf{F}}_{x2,i+1/2,j,k}^{n}(\mathbf{Q}_{i,j,k}^{(1)})\right)
\end{aligned}
$$

$$\mathbf{Q}_{i,j,k}^{t+\Delta t} \;=\; \mathbf{Q}_{i,j,k}^{(0)} + \frac{\Delta t}{\Delta x_3} \left(\tilde{\mathbf{F}}_{x3,i-1/2,j,k}^{n}(\mathbf{Q}_{i,j,k}^{(2)}) - \tilde{\mathbf{F}}_{x3,i+1/2,j,k}^{n}(\mathbf{Q}_{i,j,k}^{(2)}) \right). \tag{7}$$

In equation (7) we have used the superscript in parenthesis to denote intermediate states between direction sweeps. The ordering of the component directions (x_1, x_2, x_3) cycles over different permutations of the three coordinate directions on successive time-steps. In two dimensions the ordering is $[(x,y),(y,x)]$ and in three dimensions we have found the most consistent results by cycling over both the cyclic and anti-cyclic permutations:

$$[(x,y,z),(z,x,y),(y,z,x),(z,y,x),(x,z,y),(y,x,z)]$$

The subject of the following subsections is the procedure to compute the numerical flux which is comprised of three steps 1) reconstruction (interpolation) to zone edges §2.1, 2) upwinding the solution of the Riemann problem at each zone edge §2.2, and 3) temporal evolution of the field of conserved quantities §2.3. Our code implements several methods for carrying out each of these steps which may be utilized in the combination that best tailors the integration strategy to the requirements of the application at hand.

2.1. Spatial Reconstruction

We construct a spatially second order accurate integration procedure via suitable reconstruction of the state in each computational cell from the volume average state within that cell and its neighbors. We define a "primitive variable" operator, $L_p(\mathbf{Q}_i) = \mathbf{P}_i = [\rho, v_x, v_y, v_z, E - \rho \mathbf{v}^2/2 - \mathbf{B}^2/2, B_x, B_y, B_z]^T$, which converts the conserved state variables into a form more suitable for interpolation. Interpolation of the primitive variables, rather than the conserved, has the advantage that the reconstructed state at grid edges are guaranteed to have non-negative pressure. We write the reconstruction from the volume-average state variables collated at grid centers to the grid interface as:

$$\mathbf{P}_{L,i+1/2} = \mathbf{P}_i + \frac{1}{2}\phi_{+,i}$$
$$\mathbf{P}_{R,i-1/2} = \mathbf{P}_i - \frac{1}{2}\phi_{-,i}. \tag{8}$$

Figure 1 shows a cartoon schematic of the volume average field of primitive variables on a one dimensional grid (solid lines), the cell reconstruction (dotted lines) and the location of the left and right restricted states.
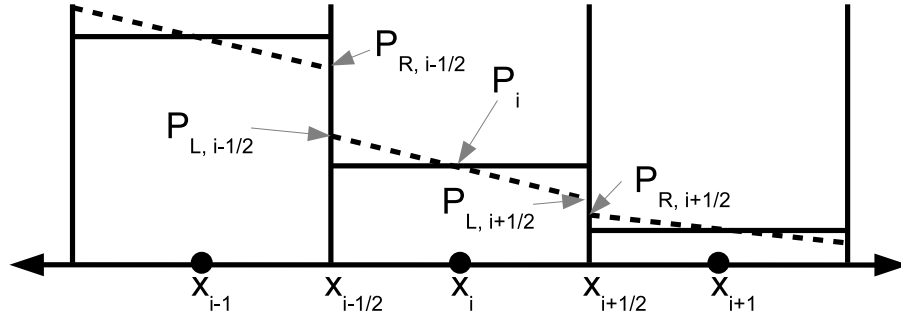
Fig. 1.— Schematic of diagram of the volume average field of primitive variables on a one dimensional grid (solid lines), the cell reconstruction (dotted lines) and the location of the left and right restricted states, P_L and P_R.

The grid interface conservative fields are then computed as

$$\begin{aligned}
\mathbf{Q}_{L,i-1/2} &= L_p^{-1}(\mathbf{P}_{L,i-1/2}) \\
\mathbf{Q}_{R,i-1/2} &= L_p^{-1}(\mathbf{P}_{R,i-1/2}).
\end{aligned} \tag{9}$$

The code implements a user selectable choice of three different second order spatial reconstruction methods. The first is the MUSCL reconstruction method of Van Leer (1979) using a slope limiter to maintain monotonicity,

$$\phi_{\pm,i} = \text{LIMITER}\left(\mathbf{P}_i - \mathbf{P}_{i-1}, \mathbf{P}_{i+1} - \mathbf{P}_i\right). \tag{10}$$

Many limiter functions may be constructed. AstroBEAR implements a choice of three limiters, which operate on the state vector parameters in equation 10 in a component-wise fashion. In order of decreasing levels of diffusion introduced into the scheme, these limiters are the "min-mod" limiter,

$$\text{MINMOD}(x,y) = \begin{cases} 0 & \text{if } xy < 0 \\ \text{MIN}(\text{ABS}(x), \text{ABS}(y))\text{SIGN}(x) & \text{otherwise} \end{cases}, \tag{11}$$

the limiter of vanLeer

$$\text{VL}(x,y) = \begin{cases} 0 & \text{if } xy < 0 \\ 2\frac{xy}{x+y} & \text{otherwise} \end{cases}, \tag{12}$$

and the "monotonized-centered" limiter

$$\text{MC}(x,y) = \begin{cases} 0 & \text{if } xy < 0 \\ \text{MIN}(2x, \frac{1}{2}(x+y), 2y) & \text{otherwise} \end{cases}. \tag{13}$$

The second reconstruction method is the local hyperbolic harmonic variation of the piecewise hyperbolic method (PHM) of Marquina (1994). The PHM reconstruction prescribes the components of $\phi_{\pm,i}$ as

$$\phi_{\pm,i} = \begin{cases} 0 & \text{if } |\delta_L| < 10^{-14} \text{ and } |\delta_R| < 10^{-14} \\ d\,\Delta x\,\eta_\pm & \text{otherwise} \end{cases} \tag{14}$$

where

$$\eta_\pm = \begin{cases} 1 & \text{if } |\kappa| < 10^{-5} \\ 2\kappa^{-2}\left(\log\left(\frac{2\mp\kappa}{2\pm\kappa}\right) \pm \frac{2\kappa}{2\mp\kappa}\right) & \text{otherwise} \end{cases}$$

$$\kappa = 2\begin{cases} \sqrt{\frac{2}{1+\Delta x}} - 1 & \text{if } |\delta_L| < 10^{-14} \quad \text{or } (\delta_L\delta_R \geq 0 \text{ and } \delta_R \leq \delta_L) \\ 1 - \sqrt{\frac{2}{1+\Delta x}} & \text{if } |\delta_R| < 10^{-14} \quad \text{or } (\delta_L\delta_R \geq 0 \text{ and } \delta_L \leq \delta_R) \\ \begin{cases} \sqrt{\frac{d}{\delta_L}} - 1 & \text{if } \delta_L \leq \delta_R \\ 1 - \sqrt{\frac{d}{\delta_R}} & \text{otherwise} \end{cases} & \text{otherwise} \end{cases}$$

$$d = 2 \begin{cases} \delta_R \left(\frac{\Delta x^2}{1+\Delta x^2} \right) & \text{if } |\delta_L| < 10^{-14} \quad \text{or } (\delta_L \delta_R \geq 0 \text{ and } \delta_R \leq \delta_L) \\ \delta_L \left(\frac{\Delta x^2}{1+\Delta x^2} \right) & \text{if } |\delta_R| < 10^{-14} \quad \text{or } (\delta_L \delta_R \geq 0 \text{ and } \delta_L \leq \delta_R) \\ \frac{\delta_R \delta_L}{\delta_R + \delta_L} & \text{otherwise,} \end{cases}$$

$$\delta_L = \frac{P_i - P_{i-1}}{\Delta x}$$

and

$$\delta_R = \frac{P_{i+1} - P_i}{\Delta x}$$

Note that η has a removable singularity about $\kappa = 0$ with $\lim_{\kappa \to 0^+}(\eta) = \lim_{\kappa \to 0^-}(\eta) = 1$. When evaluated with 8-byte precision, the expression for η begins to diverge from its true solution for $|\kappa| < 10^{-5}$ and we set $\eta \to 1$ in this region using the piecewise expression given above.

The third method is the reconstruction procedure of the piecewise parabolic method (PPM) of Colella (1984). A detailed overview of the PPM method is available from Miller & Colella (2002), and Mignone et al. (2005). Appendix B of Mignone et al. (2005) already provides a concise description of the PPM reconstruction procedure which we do not repeat here. We note that in the numerical examples using the PPM reconstruction presented later in this paper, we have taken a different approach to numerical oscillations than Mignone et al. (2005). In particular, we maintain monotonicity via the MINMOD limiter (equation 11), rather than the more compressive Van Leer limiter and we do not included the dissipation mechanisms of §B.1 of Mignone et al. (2005).

2.2. Upwinded Numerical Flux

The numerical flux is computed by upwinding the waves associated with the Riemann problem defined by $\mathbf{Q}_{L,i-1/2}$ on the left and $\mathbf{Q}_{R,i-1/2}$ on the right of each computational cell interface. AstroBEAR implements three different methods for computing the upwinded flux, the HLLD flux as described in as described in Miyoshi & Kusano (2005) the Roe flux, and the Marquina flux.

The Roe flux method Roe (1986) calls for the decomposition of the cell edge states into eigenmodes of a linearized system matrix. In the case of MHD we utilize the approximate linearized Riemann solver of Ryu & Jones (1995). We write this decomposition in terms of the eigenvalues $a_m(Q)$, right eigenvectors $\mathbf{R}_m(Q)$ and left eigenvectors $\mathbf{L}_m(Q)$ given in §2.2 of Ryu & Jones (1995) where the subscript m denotes the mth eigenmode. Singularities which arise, in certain limiting cases, in the normalization of the eigensystem are avoided in the manner prescribed by Roe & Balsara (1996). The inter-cell flux across cell boundaries

at constant x is computed as

$$
\begin{aligned}
\tilde{\mathbf{F}}_{x,i-1/2} \;=\;& \frac{1}{2}\left(\mathbf{F}_x(\mathbf{Q}_{L,i-1/2}) + \mathbf{F}_x(\mathbf{Q}_{R,i-1/2})\right) - \\
& \frac{1}{2}\sum_{m=1}^{8}\mathbf{L}_{m,i-1/2}\left(a_{m,i}\left[\mathbf{Q}_{R,i-1/2} - \mathbf{Q}_{L,i-1/2}\right]\right)\mathbf{R}_{m,i-1/2}.
\end{aligned}
\tag{15}
$$

where the eigendecomposition is carried out about a suitable average of the states to the left and right of the cell interface which we denote as $<\mathbf{Q}_{L,i-1/2},\mathbf{Q}_{R,i-1/2}>$.

$$
\begin{aligned}
a_{m,i-1/2} &= a_m(<\mathbf{Q}_{L,i-1/2},\mathbf{Q}_{R,i-1/2}>) \\
\mathbf{L}_{m,i-1/2} &= \mathbf{L}_m(<\mathbf{Q}_{L,i-1/2},\mathbf{Q}_{R,i-1/2}>) \\
\mathbf{R}_{m,i-1/2} &= \mathbf{R}_m(<\mathbf{Q}_{L,i-1/2},\mathbf{Q}_{R,i-1/2}>)
\end{aligned}
\tag{16}
$$

The flux functions of Donat & Marquina (1996), first proposed by Shu & Osher (1989) for scalar equations, take the form

$$
\tilde{\mathbf{F}}_{x,i-1/2} = \sum_{m=1}^{8}\alpha_{i-1/2}^{L}\mathbf{R}_{m,i-1/2}^{L} + \alpha_{i-1/2}^{R}\mathbf{R}_{m,i-1/2}^{R}
\tag{17}
$$

$$
\alpha_{i-1/2}^{L} = \begin{cases}
\sum_{m=1}^{8}\mathbf{L}_{m,i-1/2}^{L}\mathbf{F}(\mathbf{Q}_{L,i-1/2}) & \text{if } a_{m,i-1/2}^{L}a_{m,i-1/2}^{R} > 0 \\
& \text{and } a_{m,i-1/2}^{L} > 0 \\
0 & \text{if } a_{m,i-1/2}^{L}a_{m,i-1/2}^{R} > 0 \\
& \text{and } a_{m,i-1/2}^{L} \le 0 \\
\frac{1}{2}\sum_{m=1}^{8}\text{MAX}\left(|a_{m,i-1/2}^{L}|,|a_{m,i-1/2}^{R}|\right)\mathbf{L}_{m,i-1/2}^{L}\mathbf{Q}_{L,i-1/2} & \text{otherwise}
\end{cases}
\tag{18}
$$

$$
\alpha_{i-1/2}^{R} = \begin{cases}
0 & \text{if } a_{m,i-1/2}^{L}a_{m,i-1/2}^{R} > 0 \\
& \text{and } a_{m,i-1/2}^{L} > 0 \\
\sum_{m=1}^{8}\mathbf{L}_{m,i-1/2}^{R}\mathbf{F}(\mathbf{Q}_{R,i-1/2}) & \text{if } a_{m,i-1/2}^{L}a_{m,i-1/2}^{R} > 0 \\
& \text{and } a_{m,i-1/2}^{L} \le 0 \\
\frac{1}{2}\sum_{m=1}^{8}\text{MAX}\left(|a_{m,i-1/2}^{L}|,|a_{m,i-1/2}^{R}|\right)\mathbf{L}_{m,i-1/2}^{R}\mathbf{Q}_{L,i-1/2} & \text{otherwise}
\end{cases}
\tag{19}
$$

The numerical flux across cell boundaries at constant y, $\tilde{\mathbf{F}}_{y,j-1/2}$, and z, $\tilde{\mathbf{F}}_{z,k-1/2}$, are computed in the analogous manner. In this case a separate eight decomposition of the system matrix on each side of the cell interface is required.

$$
\begin{aligned}
a_{m,i-1/2}^{L} &= a_m(\mathbf{Q}_{L,i-1/2}) \\
a_{m,i-1/2}^{R} &= a_m(\mathbf{Q}_{R,i-1/2}) \\
\mathbf{L}_{m,i-1/2}^{L} &= \mathbf{L}_m(\mathbf{Q}_{L,i-1/2}) \\
\mathbf{L}_{m,i-1/2}^{R} &= \mathbf{L}_m(\mathbf{Q}_{R,i-1/2}) \\
\mathbf{R}_{m,i-1/2}^{L} &= \mathbf{R}_m(\mathbf{Q}_{L,i-1/2}) \\
\mathbf{R}_{m,i-1/2}^{R} &= \mathbf{R}_m(\mathbf{Q}_{R,i-1/2})
\end{aligned}
\tag{20}
$$

In the coarse of carrying out simulations in the hydrodynamic limit, we have found the Marquina flux to be advantageous for modeling certain astrophysical phenomena (discussed below). However, the method fails to converge for some MHD shock tube test problems that give rise to compound structures, that is, structures composed of a shock and rarefaction of the same wave family moving together (Brio & Wu 1988). In particular, the method fails to converge for the Riemann problem discussed in §5 of Ryu & Jones (1995). We have overcome this deficiency by constructing an adaptation of Marquina's flux which introduces a small amount of numerical diffusion by utilizing the same averaging procedure as the flux formula of Roe (1986),

$$
\begin{aligned}
a^L_{m,i-1/2} &= a_m(\mathbf{Q}_{L,i-1/2}) \\
a^R_{m,i-1/2} &= a_m(\mathbf{Q}_{R,i-1/2}) \\
\mathbf{L}^L_{m,i-1/2} = \mathbf{L}^R_{m,i-1/2} &= \mathbf{L}_m(< \mathbf{Q}_{L,i-1/2}, \mathbf{Q}_{R,i-1/2} >) \\
\mathbf{R}^L_{m,i-1/2} = \mathbf{R}^R_{m,i-1/2} &= \mathbf{R}_m(< \mathbf{Q}_{L,i-1/2}, \mathbf{Q}_{R,i-1/2} >).
\end{aligned}
\tag{21}
$$

For the methods calling for the decomposition of a linearized approximation to the system matrix (the Roe flux and our adaptation of the Marquina flux), we use the arithmetic average method of Ryu & Jones (1995) where the system is linearized at the cell interface as

$$
< \mathbf{P}^{RJ}_{i-1/2} > = (\mathbf{P}^{RJ}_{L,\ i-1/2} + \mathbf{P}^{RJ}_{R,\ i-1/2})/2.
\tag{22}
$$

Numerical tests have shown that averaging the net of the magnetic and thermal pressure rather than the thermal pressure alone provides more accurate results. Therefore we set

$$
\mathbf{P}^{RJ} = \left[\rho, v_x, v_y, v_z, P + \mathbf{B^2}/2, B_x, B_y, B_z\right]^T.
\tag{23}
$$

In the puerly hydrodynamic limit the code uses the average state of Roe (1981). This averaging guarantees desirable property that

$$
\frac{\partial \mathbf{F}(< \mathbf{Q}_{L,i-1/2}, \mathbf{Q}_{R,i-1/2} >)}{\partial \mathbf{Q}(\mathbf{Q}_L - \mathbf{Q}_R)} = \mathbf{F}_x(\mathbf{Q}_L) - \mathbf{F}_x(\mathbf{Q}_R)
\tag{24}
$$

which is not true, in general, for the arithmetic average linearization. We therefore employ the arithmetic average linearization of Ryu & Jones (1995) for MHD applications and revert to the Roe average linearization only for purely hydrodynamic applications.

In general, the Roe flux provides the least diffusive formulation. This is because the flux formulations based on the method of Donat & Marquina (1996) revert to the more diffusive local Lax-Freidrichs upwinding for transonic eigenmodes. This additional component of numerical diffusion is is advantageous for simulating certain astrophysical phenomena. It

is sufficient to prevent the development of rarefaction shocks without the need to introduce an "entropy fix" (Harten et al. 1976). It is also sufficient to dampen the development of carbuncles, even-odd decoupling and related numerical pathologies (Sutherland et al. 2003) that are particularly problematic in grid-aligned flows which exhibit strong radiative cooling.

2.3. Temporal Reconstruction

The temporal update operation for the grid centered values is given by equation 6. Replacing $n \to t$ and utilizing any of the methods for computing the numerical flux in the previous section achieves an integration that is first order in time. We implement four different methods to obtain second order temporal accuracy by performing this update using time-centered estimates of the numerical flux.

The MUSCL-Hancock predictor-corrector temporal discretization achieves second order accuracy by advancing the grid-face interpolated states by a half-time-step using a one dimensional predictor step. The predictor step is carried forward according to:

$$
\begin{aligned}
\mathbf{Q}_{L,i+1/2}^{t+\Delta t/2} &= \mathbf{Q}_{L,i+1/2}^{t} + \frac{\Delta t}{2\Delta x}\left(\mathbf{F}_x(\mathbf{Q}_{R,i-1}^t) - \mathbf{F}_x(\mathbf{Q}_{L,i+1}^t)\right) + \frac{\Delta t}{2}\mathbf{S}(\mathbf{Q}_i) \\
\mathbf{Q}_{R,i-1/2}^{t+\Delta t/2} &= \mathbf{Q}_{R,i-1/2}^{t} + \frac{\Delta t}{2\Delta x}\left(\mathbf{F}_x(\mathbf{Q}_{R,i-1}^t) - \mathbf{F}_x(\mathbf{Q}_{L,i+1}^t)\right) + \frac{\Delta t}{2}\mathbf{S}(\mathbf{Q}_i).
\end{aligned}
\tag{25}
$$

Note that the predictor step uses the cell centered, volume average fluxes. The Riemann problem at the cell interfaces is not solved and the upwinded flux at the cell-faces are not needed for this step.

The MUSCL-Hancock corrector step calls for the construction of a second order, time centered numerical flux which is computed by applying any of the upwinding procedures of (§2.2) using $\mathbf{Q}_{L,i-1/2}^{t+\Delta t/2}$, and $\mathbf{Q}_{R,-1/2}^{t+\Delta t/2}$ as the left and right states for the Riemann problem at the $i-1/2$ cell interface. We note the update to the time centered state described here, use of this procedure in more than one dimension requires the application of the operator split integrator to retain the second order accuracy of the scheme for multidimensional flow. The fully second order accurate update is therefore carried out via application of equation 7 with the time centered flux with n=dt/2

The application of the predictor-corrector schemes like the MUSCL-Hancock approach described above will in some cases necessitate the application of a protection procedure to ensure pressure and density positivity of the predictor interface states:

$$
\begin{aligned}
\rho_{L,i-1/2}^{t+\Delta t/2} &\leftarrow \text{MAX}(\rho_{L,i-1/2}^{t+\Delta t/2}, 10^{-2}\text{MIN}(\rho_{L,i-1/2}^t + \rho_{R,i-1/2}^t), 10^{-14}) \\
\rho_{R,i-1/2}^{t+\Delta t/2} &\leftarrow \text{MAX}(\rho_{R,i-1/2}^{t+\Delta t/2}, 10^{-2}\text{MIN}(\rho_{L,i-1/2}^t + \rho_{R,i-1/2}^t), 10^{-14})
\end{aligned}
$$

$$P_{L,i-1/2}^{t+\Delta t/2} \quad \leftarrow \quad \text{MAX}(P_{L,i-1/2}^{t+\Delta t/2}, 10^{-4}\text{MIN}(P_{L,i-1/2}^t + P_{R,i-1/2}^t), 10^{-14})$$
$$P_{R,i-1/2}^{t+\Delta t/2} \quad \leftarrow \quad \text{MAX}(P_{R,i-1/2}^{t+\Delta t/2}, 10^{-4}\text{MIN}(P_{L,i-1/2}^t + P_{R,i-1/2}^t), 10^{-14}). \quad (26)$$

The second temporal integration option implemented in the code is the two step Runge-Kutta temporal update operator of Shu (1988). In the first step $\tilde{\mathbf{F}}_{x,i-1/2}^t$ and $\mathbf{Q}_{x,i-1/2}^{t+\Delta t}$ are computed via the application of a first order update step given by equation 6 with $n = \Delta t$ and any operator split microphysical effects (e.g., source terms). In the second step $\tilde{\mathbf{F}}(\mathbf{Q}_{x,i-1/2}^{t+\Delta t})$ is computed by a second application of the spatial interpolation and upwinding procedure on the grid of $\mathbf{Q}_{x,i-1/2}^{t+\Delta t}$ data. The second order, time centered fluxes are then computed via the interpolation formula,

$$\tilde{\mathbf{F}}_{x,i-1/2}^{t+\Delta t/2} = \frac{1}{2}\left(\tilde{\mathbf{F}}(\mathbf{Q}_{x,i-1/2}^t) + \tilde{\mathbf{F}}(\mathbf{Q}_{x,i-1/2}^{t+\Delta t})\right). \quad (27)$$

This flux may be used to carry forward a fully second order, unsplit update via equation 6. The unsplit nature of the Runge-Kutta time stepping is a significant advantage of the method. The Runge-Kutta scheme also has a comparative advantage in that it is pressure positivity-preserving and therefore more robust. However, the method entails somewhat greater computational cost due to the solution of twice the number of Riemann problems per grid cell per time step as the MUSCL-Hancock approach. In addition the scheme suffers a somewhat restrictive time-step stability condition. The maximum numerically stable time-step Δt is computed in terms of the Courant condition as

$$\Delta t < MAX[(\frac{a_{m,i-1/2,j,k}}{\Delta x}) + MAX(\frac{a_{m,i,j-1/2,k}}{\Delta y}) + MAX(\frac{a_{m,i,j,k-1/2}}{\Delta z}) \text{ for all } i,j,k]. \quad (28)$$

In practice, we estimate the next time-step increment from the maximum wave speed encountered during the preceding integration sweeps as:

$$dt_{next} = CFL \; MAX[(\frac{a_{m,i-1/2,j,k}}{\Delta x}, \frac{a_{m,i,j-1/2,k}}{\Delta y}, \frac{a_{m,i,j,k-1/2}}{\Delta z}) \text{ for all } i,j,k]. \quad (29)$$

where CFL is a user tunable parameter. We typically choose, $CFL \sim 0.8$ for one dimensional calculations and $CFL \sim 0.4$ for multidimensional problems. Future revisions of the code will include the multidimensional corner transport upwind (CTU) reconstruction method of Colella (1990) and enhancements to this method for the integration of the MHD equations by Gardiner & Stone (2005). By explicitly including the effect of transverse-propagating waves at each grid interface, the CTU scheme retains numerical stability for larger time-steps, $CFL < 1$, while capturing greater accuracy.

2.4. Constrained Transport Scheme

While Faraday's law (equation 3) guarantees solenoidality of $\partial B/\partial t$, and therefore the maintenance of solenoidal magnetic field topologies, the Gudonov-based conservative field update procedures described in the previous section do not provide any such guarantee. This is because no provision has been made in the construction of the integration procedure that would enforce the divergence constraint on the magnetic field. Each of the fluxes used in the conservative update procedure, are second order approximations to the exact area averaged fluxes where

$$
\begin{aligned}
\mathbf{F_x} &= \tilde{\mathbf{F}}_\mathbf{x} + \mathbf{O}(\Delta x^3) \\
\mathbf{F_y} &= \tilde{\mathbf{F}}_\mathbf{y} + \mathbf{O}(\Delta y^3) \\
\mathbf{F_z} &= \tilde{\mathbf{F}}_\mathbf{z} + \mathbf{O}(\Delta z^3).
\end{aligned}
\tag{30}
$$

Therefore, the divergence of the magnetic field after a conservative update will also contain high order truncation errors, with $\nabla \cdot \mathbf{B} = \mathbf{O}(\Delta x^3) + \mathbf{O}(\Delta y^3) + \mathbf{O}(\Delta z^3)$. Local departures from $\nabla \cdot \mathbf{B} = 0$ usually grow rapidly, causing anomalous magnetic forces and unphysical plasma transport which eventually destroys the correct dynamics of the flow (Brackbill & Barnes 1980). Two strategies have emerged for adapting Godunov-based MHD schemes so that the divergence-free constraint is exactly maintained. In the first approach a projection operator is devised, usually by solving a Poisson equation which removes numerical divergences from the grid (Balsara 1998; Jiang & Wu 1999; Kim et al. 1999; Zachary et al. 1994; Ryu et al. 1995). Solving the Poisson equation is somewhat computationally expensive and particularly algorithmically complex on AMR grid hierarchies. The second approach utilizes a more multidimensional approach toward the numerical quadrature of Faraday's law by utilizing a conservative formulation of Stoke's theorem to represent magnetic field components at staggered collocation points (Balsara & Spicer 1999; Dai & Woodward 1998; Ryu et al. 1998). Following the nomenclature first commissioned by Evans & Hawley (1988), this approach is commonly referred to as "constrained transport" (CT) in the literature. The AstroBEAR code utilizes the CT approach to maintain a divergence free field, primarily due to the limitations of the first approach in AMR applications. Furthermore, Balsara & Kim (2004) have demonstrated the superiority of the staggered grid approach in the context of a stringent astrophysically motivated test problem involving the interplay of strong shocks with radiative cooling.

The basis of the constrained transport approach is realized by applying of Stoke's theorem to Faraday's law and integrating over each face of a control volume. This yields an expression for the face-average normal component of $\partial B/\partial t$ at each control volume interface. Spatial discretization of the line integral around the control volume interfaces calls for the

average electric field parallel to each edge of the control volume. Temporal discretization reveals an explicit update procedure for the normal component of the magnetic field at each computational volume interface. The resulting discretized equations,

$$
\begin{aligned}
B^{t+\Delta t}_{x,i-1/2,j,k} &= B^{t}_{x,i-1/2,j,k} + \frac{\Delta t}{\Delta y \Delta z} \\
&\quad \left(\Delta y E_{y,i-1/2,j,k+1/2} - \Delta y E_{y,i-1/2,j,k-1/2} - \right.\\
&\quad \left. \Delta z E_{z,i-1/2,j+1/2,k} + \Delta z E_{z,i-1/2,j-1/2,k} \right) \\
B^{t+\Delta t}_{y,i,j-1/2,k} &= B^{t}_{y,i,j-1/2,k} + \frac{\Delta t}{\Delta x \Delta z} \\
&\quad \left(\Delta z E_{z,i+1/2,j-1/2,k} - \Delta z E_{z,i-1/2,j-1/2,k} - \right.\\
&\quad \left. \Delta x E_{x,i,j-1/2,k+1/2} + \Delta x E_{x,i,j-1/2,k-1/2} \right) \\
B^{t+\Delta t}_{z,i,j,k-1/2} &= B^{t}_{z,i,j,k-1/2} + \frac{\Delta t}{\Delta x \Delta y} \\
&\quad \left(\Delta x E_{x,i,j+1/2,k-1/2} - \Delta x E_{x,i,j-1/2,k-1/2} - \right.\\
&\quad \left. \Delta y E_{y,i+1/2,j,k-1/2} + \Delta y E_{y,i-1/2,j,k-1/2} \right).
\end{aligned}
\tag{31}
$$

gives the desired CT update operator. Note that the centered difference discretization of the divergence of the magnetic field,

$$
(\nabla \cdot \mathbf{B})_{i,j,k} = \frac{B_{x,i+1/2,j,k} - B_{x,i-1/2,j,k}}{\Delta x} + \frac{B_{y,i,j+1/2,k} - B_{y,i,j-1/2,k}}{\Delta y} + \frac{B_{z,i,j,k+1/2} - B_{z,i,j,k-1/2}}{\Delta z}
\tag{32}
$$

is preserved

$$
(\nabla \cdot \mathbf{B})^{t+dt}_{i,j,k} = (\nabla \cdot \mathbf{B})^{t}_{i,j,k}
\tag{33}
$$

and the CT update operator maintains a divergence free representation of the magnetic field provided that the initial magnetic field is divergence-free. We emphasize that the CT update procedure requires that the components of the magnetic field be collated at the center of the zone faces to which they are orthogonal and that the component of the electric field parallel to each computational cell interface be known. The spatial location of the desired electric and magnetic field components are illustrated in figure 2.
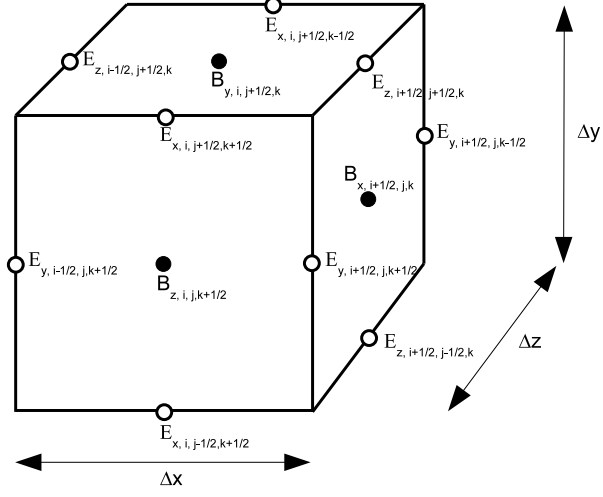
Fig. 2.— The location of the staggered electric and magnetic field components on a computational cell centered at position i, j, k.

Specification of the CT update procedure is completed via a suitable construction of the required electric field components at each grid edge. The fluxes of the MHD equation (equation 2) can be expressed in terms of the electric field using Ohm's law (equation 4). The numerical inter-cell fluxes computed during the conservative update step described in the preceding subsections, provide a second order, shock capturing approximation to the components of the electric field at the center of each computational cell interface. The CT update scheme, however, calls for the electric field at the grid edges. A reconstruction of the cell-face electric fields to the cell edges that retains second order accuracy is given by:

$$
\begin{aligned}
E_{x,i,j-1/2,k-1/2}^{t+\Delta t/2} &= k\left(\tilde{f}_{z\ 7,i,j,k-1/2}^{t+\Delta t/2} + \tilde{f}_{z\ 7,i,j-1,k-1/2}^{t+\Delta t/2} - \tilde{f}_{y\ 8,i,j-1/2,k}^{t+\Delta t/2} - \tilde{f}_{y\ 8,i,j-1/2,k-1}^{t+\Delta t/2}\right) \\
E_{y,i-1/2,j,k-1/2}^{t+\Delta t/2} &= k\left(\tilde{f}_{x\ 8,i-1/2,j,k}^{t+\Delta t/2} + \tilde{f}_{x\ 8,i-1/2,j,k-1}^{t+\Delta t/2} - \tilde{f}_{z\ 6,i,j,k-1/2}^{t+\Delta t/2} - \tilde{f}_{z\ 6,i-1,j,k-1/2}^{t+\Delta t/2}\right) \\
E_{z,i-1/2,j-1/2,k}^{t+\Delta t/2} &= k\left(\tilde{f}_{y\ 6,i,j-1/2,k}^{t+\Delta t/2} + \tilde{f}_{y\ 6,i-1,j-1/2,k}^{t+\Delta t/2} - \tilde{f}_{x\ 7,i-1/2,j,k}^{t+\Delta t/2} - \tilde{f}_{x\ 7,i-1/2,j-1,k}^{t+\Delta t/2}\right),\ (34)
\end{aligned}
$$

where the cell-face electric fields have been written in terms of cell interface fluxes. Setting $\tilde{f}_* = \tilde{F}_*$ and $k = 1/4$ recovers the CT scheme of Balsara & Spicer (1999). Many procedures for averaging the cell interface flux components to construct the cell-edge electric field components. The CT scheme of Ryu et al. (1998) can be expressed in the form of equation 34 by retaining only the advective part of the inter-cell flux,

$$
\begin{aligned}
\mathbf{f}_{x\ 6,7,8} &= v_x\left[0, B_y, B_z\right]^T \\
\mathbf{f}_{y\ 6,7,8} &= v_y\left[B_x, 0, B_z\right]^T \\
\mathbf{f}_{z\ 6,7,8} &= v_z\left[B_x, B_y, 0\right]^T
\end{aligned}
$$

(35)

and setting $k = 1/2$. The upwinded, time centered, cell-face fluxes $\tilde{f}_*^{t+\Delta t/2}$ are constructed from the cell centered flux components f_*^t according to the same procedure given in §2.2. This update procedure retains the upwinding abilities of the conservative update scheme while maintaining a divergence free solution to the magnetic field via the correspondence of the components of the magnetic flux with the components of the electric field called for by the CT update procedure. Construction of the electric field from the components of the intercell numerical flux therefore has the advantage of introducing very little numerical dissipation into the solution. Of the schemes tested by Tóth (2000), those that utilize this approach to reconstructing the electric field at grid edges produce the most accurate results. One implementation detail that should be noted is that the update of the components of the magnetic field collated along the boundary of the computational domain requires the flux components that are parallel to that boundary extending into the first row of ghost cells along the boundary. The conservative update procedure must therefore extend one row of computational cells into the ghost cell region during integration sweeps transverse to the boundary even though no conservative update is applied to the boundary cells. Extension

into the ghost region ensures that the components of the numerical flux required in the CT update step are computed.

At the end of each CT update step, the volume centered cell solution for the magnetic field, computed during the Gudonov update, is discarded in favor of the solution provided by the CT update. At this stage in the algorithm, the cell centered the magnetic field is recomputed according to the procedure:

$$
\begin{aligned}
\tilde{B}_{x,i,j,k} &= \frac{1}{2}\left(B_{x,i+1/2,j,k} + B_{x,i-1/2,j,k}\right) \\
\tilde{B}_{y,i,j,k} &= \frac{1}{2}\left(B_{y,i,j+1/2,k} + B_{y,i,j-1/2,k}\right) \\
\tilde{B}_{z,i,j,k} &= \frac{1}{2}\left(B_{z,i,j,k+1/2} + B_{z,i,j,k-1/2}\right).
\end{aligned}
\tag{36}
$$

Even though the solution of the magnetic field is advanced in time at cell interfaces, we retain the grid of volume average magnetic field components in order to compute the magnetic pressure at the cell centers. Also, the volume average magnetic field and total energy are synchronized with the cell-face magnetic field after every CT update step in order to preserve the volume averaged thermal energy.

$$
\tilde{\mathcal{E}}_{i,j,k} \leftarrow \mathcal{E}_{i,j,k} - \frac{\mathbf{B}_{i,j,k}^2}{2} + \frac{\tilde{\mathbf{B}}_{i,j,k}^2}{2}
\tag{37}
$$

The total energy is thereby adjusted such that the CT update preserves thermal energy. This optional step avoids numerical difficulty with negative thermal pressure that arise in strongly magnetized problems at the expense of energy conservation. We view this as an acceptable trade-off, particularly for astrophysical applications that are not energy conserving due to radiative energy losses.

Because the normal component of the magnetic field is known at cell faces, it is not necessary to interpolate these values during the spatial reconstruction step of §2.1. Recalling that we have defined the 6th, 7th and 8th components of the primitive field vector as the x, y and z components of the magnetic field (equation 8), we set

$$
\begin{aligned}
P_{L,6,\ i-1/2} &= P_{R,6,\ i-1/2} = b_{x,i-1/2} \\
P_{L,7,\ j-1/2} &= P_{R,7,\ j-1/2} = b_{y,j-1/2} \\
P_{L,8,\ k-1/2} &= P_{R,8,\ k-1/2} = b_{z,k-1/2}
\end{aligned}
\tag{38}
$$

in lieu of the spatial reconstruction procedure when using an unsplit scheme (equation 6). With a direction split scheme (equation 7) the partial update of the cell-centered field from prior direction sweeps is interpolated back to the cell edge and added to the cell edge state

during the spatial reconstruction step (§sr) in order to retain second order accuracy with multidimensional flow

$$P_{L,6,\ i-1/2} \ = \ P_{R,6,\ i-1/2} = b_{x,i-1/2} + \frac{1}{2}(B_{x,i}^{(\iota-1)} - B_{x,i}^{(0)} + B_{x,i-1}^{(\iota-1)} - B_{x,i-1}^{(0)})$$

$$P_{L,7,\ j-1/2} \ = \ P_{R,7,\ j-1/2} = b_{y,j-1/2} + \frac{1}{2}(B_{y,j}^{(\iota-1)} - B_{y,j}^{(0)} + B_{y,j-1}^{(\iota-1)} - B_{y,j-1}^{(0)})$$

$$P_{L,8,\ k-1/2} \ = \ P_{R,8,\ k-1/2} = b_{z,k-1/2} + \frac{1}{2}(B_{z,k}^{(\iota-1)} - B_{z,k}^{(0)} + B_{z,k-1}^{(\iota-1)} - B_{z,k-1}^{(0)}) \qquad (39)$$

where the superscript $(\iota-1)$ refers to the state after the previous direction sweep. While this procedure does maintain the second order accuracy achieved via direction splitting it does suffer from the flaw that the reconstructed states are not exactly divergence free. Instead, the reconstructed states given by MUSCL-Hancock time stepping procedure described in §2.3 and any direction split scheme suffers from the undesirable property that,

$$(b_{x,i-1/2}^{t+dt/2} - b_{x,i-1/2}^{t+dt/2})/dx + (b_{y,i-1/2}^{t+dt/2} - b_{y,i-1/2}^{t+dt/2})/dy + (b_{z,i-1/2}^{t+dt/2} - b_{z,i-1/2}^{t+dt/2})/dz = 0 \qquad (40)$$

is not maintained exactly. Also note that the CT update procedure is applied after each stage of the multistage Runge-Kutta temporal update procedure such described in §2.3.

We generally find the divergence error introduced via the split reconstruction procedure is small and that because we apply a divergence free CT update for the magnetic field, the effect of this small error does not grow rapidly. The effect of this error appears as inexact evolution of the z-component of the magnetic field in the magnetic field loop advection test of Gardiner & Stone (2005) as shown in §5.2. Gardiner & Stone (2005) introduced a two dimensional unsplit scheme and later a three dimensional extension thereof Gardiner & Stone (2008) where they devise an unsplit reconstruction that is not subject to this error at the expense of considerably increased algorithmic and computational complexity. Balsara (2004) has shown that unsplit MHD schemes are less diffusive in some tests than the dimensionally split counterpart. Because of this we recommend the dimensionally unsplit Runge-Kutta scheme which does provide for exactly divergence free reconstructed states for AtroBEAR MHD applications. Never the less the direction split MUSCL-Hancock update has proven to be reliable in earlier purely hydrodynamic works (Cunningham et al. 2006a,b; Dennis et al. 2008; Yirak et al. 2008), and for this reason we leave this option available for MHD applications. We note that the MUSCL-Hancock scheme is efficient in terms of computational cost, requiring only one Riemann solver per grid cell per time step while retaining stability for $CFL < 1$ and that exhaustive testing of this and other (Ryu et al. 1998) direction split MHD schemes have shown good results.

2.5. Summary or Numerical Methods

The menu of options available in our code includes three spatial reconstruction methods §2.1: linear (MUSCL), piecewise hyperbolic (PHM) and piecewise parabolic (PPM), two temporal reconstruction methods §2.3: MUSCL-Hancock and Runge-Kutta, four different Riemann solvers / upwinding procedures §2.2: the HLLD flux, the Roe flux, the Marquina flux, and an adaptation of the Marquina flux that is better suited for magnetized flow involving compound wave structures and two different constrained transport schemes for preserving the solenoidality constraint on magnetized flows §2.4: the method of Balsara & Spicer (1999) and the method of Ryu et al. (1995). The user of the code may choose the method for each of these operations which are summarized in table 1. The advantage of this approach is that a given simulation may be performed using several different methods. The solution strategy which is optimal for the physical regime of a given simulation may be readily applied.

Table 1: Numerical Method Options.

Spatial Reconstruction	Temporal Reconstruction	Flux Function	CT Scheme
MUSCL	MUSCL-Hancock	Roe	Ryu et al.
PHM	Runge-Kutta	Marquina	Balsara & Spicer
PPH		Adapted Marquina	
		HLLD	

3. Adaptive Mesh Refinement

The central feature of the BEARCLAW framework on which AstroBEAR is based is that it provides a framework for Adaptive Mesh refinement (AMR). Under AMR, regions of the flow that are susceptible to large discretization errors are carried forward on a computational grid of higher resolution while flow features not requiring high resolution for adequate numerical convergence are carried forward on a computational grid of lower resolution. Two approaches to AMR have emerged: (1) the block-based method of Berger & Oliger (1984) and Berger & Colella (1989) which constructs a patchwork of refined grids that optimally covers all of the cells on the next-coarsest level that are heuristically identified for refinement (2) an alternative approach where individual computational cells are refined or derefined separately (Khokhlov 1998). Our code employs the former approach. In this section we give an overview of the AMR algorithm and stages of the AMR algorithm that require special attention in handling grid face magnetic field components. For discussion we use the term "parent grid" to designate an underlying block on the next coarser level, "parent level" to designate all of the grid blocks that are one level coarser, "child grids" to designate those grid blocks that are one level finer and "child level" to refer to grids that are of higher resolution by one refinement ratio than the current grid. Advancement of an AMR hierarchy of grids is carried out according to the pseudo-code algorithm given in appendix B. A schematic of the update procedure is shown in figure 3 for an AMR hierarchy of three levels of refinement where each level has a refinement ratio of 2. Curved horizontal arrows represent integration of all grids on a given refinement level. The algorithm is adaptive in time, with each level advanced in time increments $dt_{level} = dt_{level-1}/r$ where r is the refinement ratio of the level. Gray vertical arrows represent restriction and refluxing of the solution on refined grids to their parent level. Black vertical arrows represent prolongation of the solution from the coarse level to its parent level.
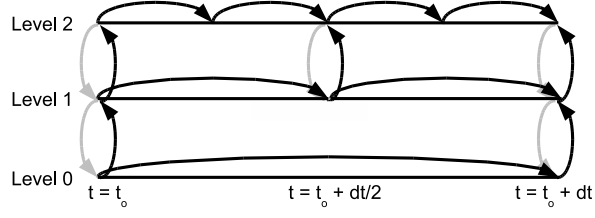
Fig. 3.— A schematic of the update procedure for an AMR hierarchy of three levels of refinement where each level has a refinement ratio of 2. Curved horizontal arrows represent integration of all grids on a given refinement level. Gray vertical arrows represent restriction of refined grids to their parent level. Black vertical arrows represent prolongation of the solution from the coarse level to its parent level.

The first step of the update procedure, "Set Ghost," calls for the initialization of the ghost cells that are exterior to all grids on the given level. Figure 4 shows an example of an AMR hierarchy containing one grid on the root level (level=0), and one refined level (level=1). The interior of each grid is delineated by solid lines and the extended grid which include the interior and ghost region of each grid are delineated by dashed lines. The face-centered magnetic field components that coincide with boundaries delineating the interior of each grid are treated as interior cells. We classify ghost cells into three categories: 1) same-level ghost cells that coincide with the interior of another grid on the same level appear white in the figure, 2) physical ghost cells that lie outside of the computational domain appear dark gray in the figure, 3) child-level ghost cells that coincide with the interior of grids on the parent level appear light gray in the figure. Same-level ghost zones are initialized to the state of the interior of the coincident grid. Physical ghost cells are initialized according to user specified boundary conditions, the code provides three physical boundary options; constant extrapolation, reflecting or periodic. The initialization of parent-level ghost cells is carried out as a part of the "Grid Adapt" procedure which will be discussed below.
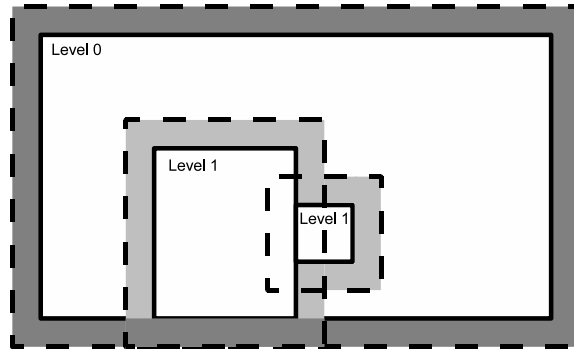
Fig. 4.— An example of an AMR hierarchy containing one grid on the root level (level=0), and one refined level (level=1). The interior of each grid is delineated by solid lines and the extended grid which include the interior and ghost region of each grid are delineated by dashed lines.

The "Grid Adapt" procedure determines the arrangement of and initialization of a new AMR hierarchy on a given level that tracks the evolution of flow features in the solution. A user-specified truncation error estimation procedure is applied to each grid that is one level coarser. AstroBEAR uses either the maximum absolute value of the primitive vector gradient or Richardson extrapolation (Berger & Oliger 1984; Berger & Colella 1989) as the options for error estimation. Zones on the parent grids with estimated error greater than a user-specified tolerance are flagged for refinement. We employ the patch-wise clustering algorithm of Berger & Rigoutsos (1991) to determine arrangement of refined grid patches that optimally overlays all of the zones flagged for refinement. For easier parallel implementation, we require that each grid has only one parent. In figure 5, the new arrangement of grid patches on the first refinement level with interior boundaries and ghost boundaries delineated by solid and dashed lines respectively. The region coinciding with the previous arrangement of AMR patches are shaded in gray. Interior regions of the new grid arrangement that coincide with interior regions of the previous patchwork of grids on the same level are initialized by copying the field values from the previous grids. The previous patchwork of grids on this level are then released from memory. The ghost zones, and interior zones that do not coincide with the interior of the previous grid patches are initialized from the parent grid via a prolongation operator. The code prolongs the cell-centered conserved fields using interpolation from the parent grid. The cell-face grid of magnetic field components are initialized using a divergence-preserving prolongation operator in order to preserve the integrity of the CT update procedure. We will discuss this operator in detail in §4.2.
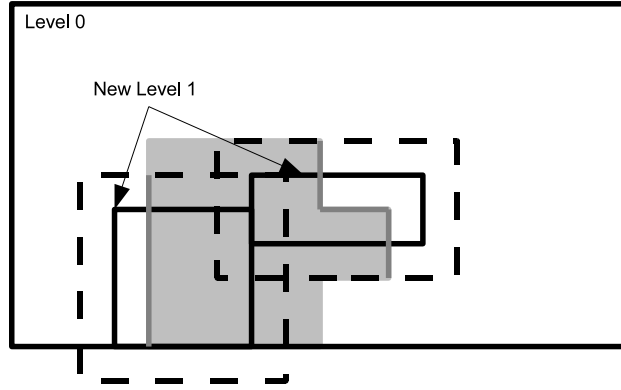
Fig. 5.— The new arrangement of grid patches on the first refinement level with interior boundaries and ghost boundaries delineated by solid and dashed lines respectively. The region coinciding with the previous arrangement of AMR patches are shaded in gray.

The "integrate" step advances the solution on each grid on the given level using one of the integration procedures discussed in §2 as specified by the user. The time-adaptive nature of the AMR engine imposes the difficulty that boundary information from parent grids is not available during each step of child grid integration cycle. As shown in figure 3 for a refinement ratio of two, child ghost zones are temporally synchronized with their parent grids only every-other time cycle. To accommodate this, we incorporate an "extended" arrangement of ghost cells. Each refined grid carries a strip of ghost zones that extends the width $r \times m_{bc}$ cells beyond the interior of the grid where r is the refinement ratio, and m_{bc} is the number of ghost cells required by the integration stencil. The MUSCL-Hancock reconstruction operator (§2.1) without direction splitting requires two ghost cells, yielding $m_{bc} = 2$. An extra ghost zone is required in multidimensional problems when using direction splitting and constrained transport in order to compute the flux components necessary to compute the EMF at the grid corners, yielding $m_{bc} = 3$. The Runge-Kutta temporal integration method (§2.3) has been implemented via additional rows of ghost cells to fully update the interior region with $m_{bc} = 4$. The update of the extended region of ghost cells is illustrated in figure 6 for a refinement ratio $r = 2$. The initial representation of the field is at time t. The first integration cycle carries all cells interior to the first ring of m_{bc} ghost zones shaded in dark gray forward in time from t to $t + dt/2$. On the second integration cycle, the interior cells shaded in dark gray are carried forward in time from t to $t + dt/2$. The second integration step can be carried out because the outermost ring of m_{bc} ghost zones are outside of the domain of influence on the interior cells.
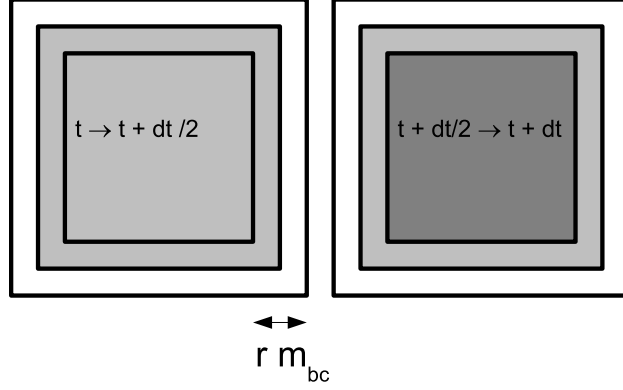
Fig. 6.— A schematic of the arrangement of the extended ghost region on a grid with a refinement ratio of 2. The initial representation of the field is at time t. The first integration cycle, illustrated in the left panel, carries all cells interior to the outer ring of m_{bc} ghost zones shaded in dark gray forward in time from t to $t + dt/2$. On the second integration cycle, illustrated in the right panel the interior cells shaded in dark gray are carried forward in time from t to $t + dt/2$.

The "Synchronize to Parent" call carries forward the synchronization of the solution on a given level to its parent grid. The synchronization procedure is composed of two steps: application of coarse to fine level refluxing and restriction of the solution. In the refluxing step, a spatio-temporal average of the flux from child grid interfaces along coarse / fine grid boundaries is compared to the flux as computed during the integration of the coarse grid. A correction is applied to the parent grid so that the effective flux across this boundary is equal to that as computed on the child grid. The restriction step calls for the coarsening and injection of field data from the interior of the child grids into their respective parent grids. We employ volume weighted average restriction of cell centered conserved fields. The restriction of face-centered magnetic field components requires special attention to maintain the divergence-free property of the magnetic field which will be discussed in the next section.

4. Divergence Preserving Restriction and Prolongation Operators

In §2.4 we discussed the importance of satisfying the $\nabla \cdot \mathbf{B} = 0$ in order to maintain the integrity of the numerical solution to the MHD equations and demonstrated an adaptation to Goduonov-based schemes that preserves the divergence of the magnetic field throughout the calculation. The use of AMR imposes an additional challenge that must be overcome to maintain the divergence of the magnetic field throughout the calculation. Specifically, the restriction step, which maintains the consistency on coarse levels with the finer levels of refinement in the grid, and the prolongation step, which initializes coarse representations of the solution to finer grids in regions that have been flagged for refinement must not introduce divergence errors into the solution. The volume average and bilinear interpolation procedures utilized for the restriction and prolongation of the cell-centered conserved fields cannot be adapted to operate on the grid-edge magnetic fields in a divergence preserving manner. Two approaches to the divergence preserving prolongation have emerged. Balsara (2001) has generalized the divergence free reconstruction procedure of Balsara & Spicer (1999) to devise a piece-wise quadratic interpolant that is divergence preserving. Li & Li (2004) present an adaptation of Balsara's procedure that simplifies its implementation for problems involving arbitrary refinement ratios. Tóth & Roe (2002) has devised a prolongation procedure by solving an algebraic system which enforces the maintenance of the volume average curl and divergence over a coarse grid cell.

In this subsections that follow, we present the restriction and prolongation formulae employed in our code. In particular, we present the prolongation procedure of (Tóth & Roe 2002) in a less compact form than that of the original authors which are more readily transcribed into computer code. To simplify implementation our code only allows refinement

ratios of two between successive levels of refinement.

4.1. Restriction

Figure 7 illustrates the locations of the magnetic field components utilized by the constrained transport update procedure where a refined grid (denoted with dotted lines) has been embedded within one coarse grid cell (denoted with solid lines) for a two dimensional calculation. We denote the magnetic field components on coarse grid faces as β, on refined cell faces that are coincident with coarse grid faces (the exterior faces) as b, and on refined cell faces that do not coincide with coarse grid faces (the interior faces) as B. We have adapted a short hand notation where the first, second, and third character in the superscript to the refined grid magnetic field components either represents the location above $(+)$, below $(-)$ or aligned with (0) the center of the coarse cell in each of the x, y, and z directions.
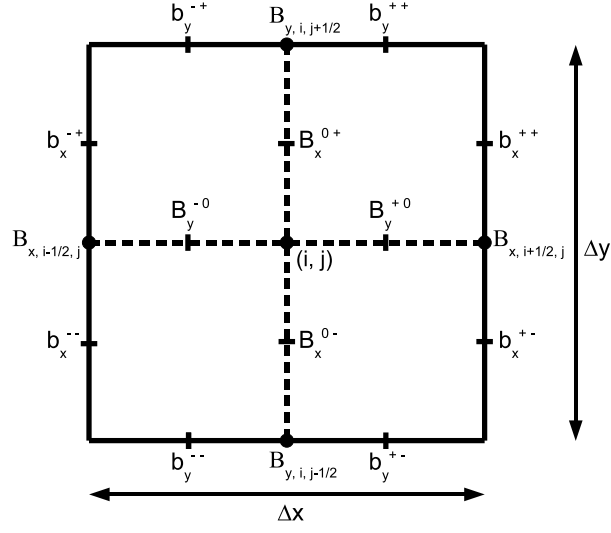
Fig. 7.— Illustration of the locations on a two dimensional grid of the staggered electric and magnetic field components with a refined grid, delineated with dotted lines, that has been embedded within one coarse grid cell, delineated by solid lines.

We require that the fine-to-coarse grid synchronization step maintain the cell interface magnetic field in an area-averaged sense,

$$
\begin{aligned}
\beta_{x,i\pm1/2,j} &= \frac{1}{2}\left(b_x^{\pm+} + b_x^{\pm-}\right) \\
\beta_{y,i,j\pm1/2} &= \frac{1}{2}\left(b_y^{+\pm} + b_y^{-\pm}\right)
\end{aligned}
\tag{41}
$$

in two dimensions, and

$$
\begin{aligned}
\beta_{x,i\pm1/2,j,k} &= \frac{1}{4}\left(b_x^{\pm++} + b_x^{\pm-+} + b_x^{\pm+-} + b_x^{\pm--}\right) \\
\beta_{y,i,j\pm1/2,k} &= \frac{1}{4}\left(b_y^{+\pm+} + b_y^{-\pm+} + b_y^{+\pm-} + b_y^{-\pm-}\right) \\
\beta_{z,i,j,k\pm1/2} &= \frac{1}{4}\left(b_z^{++\pm} + b_z^{-+\pm} + b_z^{+-\pm} + b_z^{--\pm}\right)
\end{aligned}
\tag{42}
$$

in three dimensions. Equations 41 & 42 must be satisfied while preserving the divergence of the magnetic field along coarse/fine grid boundaries. Simultaneous satisfaction of these properties along coarse/fine grid interfaces and this restriction condition is accomplished by applying a suitable restriction of the electric field from fine to coarse grids before performing the CT update (equations 31) on the coarse level. Manipulation of equations 34 subject to the constraint provided by equations 41 &42 at all times yield the desired electric field restriction operator as

$$
E_{z,i-1/2,j-1/2}^{t+dt/2} = \tfrac{1}{2}\left(e_{z,i-1/2,j-1/2}^{t+dt/4} + e_{z,i-1/2,j-1/2}^{t+3dt/4}\right),
\tag{43}
$$

in two dimensions and

$$
\begin{aligned}
E_{x,i,j-1/2,k-1/2}^{t+dt/2} &= \tfrac{1}{4}\left(e_{x,i-1/4,j-1/2,k-1/2}^{t+dt/4} + e_{x,i-1/4,j-1/2,k-1/2}^{t+3dt/4} + e_{x,i+1/4,j-1/2,k-1/2}^{t+dt/4} + e_{x,i+1/4,j-1/2,k-1/2}^{t+3dt/4}\right) \\
E_{y,i-1/2,j,k-1/2}^{t+dt/2} &= \tfrac{1}{4}\left(e_{y,i-1/2,j-1/4,k-1/2}^{t+dt/4} + e_{y,i-1/2,j-1/4,k-1/2}^{t+3dt/4} + e_{y,i-1/2,j+1/4,k-1/2}^{t+dt/4} + e_{y,i-1/2,j+1/4,k-1/2}^{t+3dt/4}\right) \\
E_{z,i-1/2,j-1/2,k}^{t+dt/2} &= \tfrac{1}{4}\left(e_{z,i-1/2,j-1/2,k-1/4}^{t+dt/4} + e_{z,i-1/2,j-1/2,k-1/4}^{t+3dt/4} + e_{z,i-1/2,j-1/2,k+1/4}^{t+dt/4} + e_{z,i-1/2,j-1/2,k+1/4}^{t+3dt/4}\right)
\end{aligned}
\tag{44}
$$

in three dimensions where $\mathbf{E}$ is the electric field on the coarse grid and $\mathbf{e}$ is electric field of the refined grid. In figure 3 note that level 0 is advanced by an increment from t to $t+dt/2$ using the electric field computed at time $t+dt/2$ in one step while the next child level, level 1, is integrated by the same increment in two steps using the electric field at time $t+dt/4$ to integrate from t to $t+dt/2$ and electric field at time $t+3dt/4$ to integrate from $t+dt/2$ to $t+dt$. The temporal averaging of the electric field is necessary due to the temporal refinement capability of the code. The time averaging in equations 43 & 44 ensures that evolution of the magnetic field across level boundaries remains divergence free and consistent in the sense of equations 41 & 42.

4.2. Prolongation

The prolongation step initializes a newly refined grid from its parent grid that is coarser by one level of refinement. The prolongation of the face centered magnetic field is carried out in two steps. In the first stage, the exterior faces that coincide with the edges of an already refined grid block are set by copying the field values from the coincident face of the already refined grid. The exterior faces that do not coincide with the edges of an already refined region are computed via a bilinear interpolation of the coarse representation of the field given by

$$
\begin{aligned}
b_x^{\pm+} &= \beta_{x,i\pm1/2,j} + \frac{1}{2}\delta_y\beta_x \\
b_x^{\pm-} &= \beta_{x,i\pm1/2,j} - \frac{1}{2}\delta_y\beta_x \\
b_y^{+\pm} &= \beta_{y,i,j\pm1/2} + \frac{1}{2}\delta_x\beta_y \\
b_y^{-\pm} &= \beta_{y,i,j\pm1/2} - \frac{1}{2}\delta_x\beta_y,
\end{aligned}
\tag{45}
$$

in two dimensions and

$$
\begin{aligned}
b_x^{\pm++} &= \beta_{x,i\pm1/2,j,k} + \frac{1}{2}(\ \delta_y\beta_x + \delta_z\beta_x) \\
b_x^{\pm+-} &= \beta_{x,i\pm1/2,j,k} + \frac{1}{2}(\ \delta_y\beta_x - \delta_z\beta_x) \\
b_x^{\pm-+} &= \beta_{x,i\pm1/2,j,k} + \frac{1}{2}(-\delta_y\beta_x + \delta_z\beta_x) \\
b_x^{\pm--} &= \beta_{x,i\pm1/2,j,k} + \frac{1}{2}(-\delta_y\beta_x - \delta_z\beta_x) \\
b_y^{+\pm+} &= \beta_{y,i,j\pm1/2,k} + \frac{1}{2}(\ \delta_x\beta_y + \delta_z\beta_y) \\
b_y^{+\pm-} &= \beta_{y,i,j\pm1/2,k} + \frac{1}{2}(\ \delta_x\beta_y - \delta_z\beta_y) \\
b_y^{-\pm+} &= \beta_{y,i,j\pm1/2,k} + \frac{1}{2}(-\delta_x\beta_y - \delta_z\beta_y) \\
b_y^{-\pm-} &= \beta_{y,i,j\pm1/2,k} + \frac{1}{2}(-\delta_x\beta_y - \delta_z\beta_y) \\
b_z^{++\pm} &= \beta_{z,i,j,k\pm1/2} + \frac{1}{2}(\ \delta_x\beta_z + \delta_y\beta_z) \\
b_z^{+-\pm} &= \beta_{z,i,j,k\pm1/2} + \frac{1}{2}(\ \delta_x\beta_z - \delta_y\beta_z) \\
b_z^{-+\pm} &= \beta_{z,i,j,k\pm1/2} + \frac{1}{2}(-\delta_x\beta_z + \delta_y\beta_z) \\
b_z^{--\pm} &= \beta_{z,i,j,k\pm1/2} + \frac{1}{2}(-\delta_x\beta_z - \delta_y\beta_z),
\end{aligned}
\tag{46}
$$

in three dimensions, where we compute the spatial jumps using the same slope limiter (equations 11-13)as the base scheme:

$$
\begin{aligned}
\delta_x\beta_* &= \text{LIMITER}(\beta_{*,i+1,j-1/2,k-1/2} - \beta_{*,i,j-1/2,k-1/2},\ \beta_{*,i,j-1/2,k-1/2} - \beta_{*,i-1,j-1/2,k-1/2}) \\
\delta_y\beta_* &= \text{LIMITER}(\beta_{*,i-1/2,j+1,k-1/2} - \beta_{*,i-1/2,j,k-1/2},\ \beta_{*,i-1/2,j,k-1/2} - \beta_{*,i-1/2,j-1,k-1/2}) \\
\delta_z\beta_* &= \text{LIMITER}(\beta_{*,i-1/2,j-1/2,k+1} - \beta_{*,i-1/2,j-1/2,k},\ \beta_{*,i-1/2,j-1/2,k} - \beta_{*,i-1/2,j-1/2,k-1})
\end{aligned}
\tag{47}
$$

In the second stage of the prolongation procedure we interpolate from the exterior faces of the refined grid cell to the interior faces. In three dimensions, the 12 refined inter-cell faces that are interior to the coarse cell are constructed via an interpolation from the magnetic field components collated at the 24 refined grid exterior face centers that coincide with a coarse cell interface. Following Tóth & Roe (2002) we construct this interpolation to satisfy the constraint that it be divergence and curl preserving. For readability and conciseness, we illustrate the steps required to derive such an interpolation procedure in detail only for the two dimensional case. We then present the analogous solution in three dimensions. The volume average divergence, computed via the application of Gauss's law around the perimeter of the exterior faces is:

$$
d^{00} = \frac{1}{2}(\bar{b}_x^{++} + \bar{b}_x^{+-} - \bar{b}_x^{-+} - \bar{b}_x^{--} + \bar{b}_y^{++} + \bar{b}_y^{-+} - \bar{b}_y^{+-} - \bar{b}_y^{--})
\tag{48}
$$

where we have used the bar accent to denote division by the discretization width in the normal direction on the coarse level (see figure 7), i.e. $\bar{b}_x = b_x/\Delta x$, and $\bar{b}_y = b_y/\Delta y$. The curl of the field is constructed by bilinear interpolation of the requisite exterior field components to the origin of the refined cell as:

$$
c_z^{00} = \frac{\Delta y}{2\Delta x}(\bar{b}_y^{++} - \bar{b}_y^{-+} + \bar{b}_y^{+-} - \bar{b}_y^{--}) - \frac{\Delta x}{\Delta y}(\bar{b}_x^{++} - \bar{b}_x^{+-} + \bar{b}_x^{-+} - \bar{b}_x^{--}).
\tag{49}
$$

The divergence centered at each of the four refined cell interiors is:

$$
\begin{aligned}
D^{--} &= 2(\bar{B}_x^{0-} - \bar{b}_x^{--} + \bar{B}_y^{-0} - \bar{b}_y^{--}) \\
D^{+-} &= 2(\bar{b}_x^{+-} - \bar{B}_x^{0-} + \bar{B}_y^{+0} - \bar{b}_y^{+-}) \\
D^{-+} &= 2(\bar{B}_x^{0+} - \bar{b}_x^{-+} + \bar{b}_y^{-+} - \bar{B}_y^{-0}) \\
D^{++} &= 2(\bar{b}_x^{++} - \bar{B}_x^{0+} + \bar{b}_y^{++} - \bar{B}_y^{+0})
\end{aligned}
\tag{50}
$$

and the curl at the origin of the refinement cells implied by the interior field values is:

$$
C_z^{00} = \frac{2\Delta y}{\Delta x}(\bar{B}_y^{+0} - \bar{B}_y^{-0}) - \frac{2\Delta x}{\Delta y}(\bar{B}_x^{0+} - \bar{B}_x^{0-}).
\tag{51}
$$

The desired interpolation procedure is determined by imposing the condition that each of the refined grid cells contributes equally to the divergence of the refinement region, $d^{00} =$

$D^{--} = D^{-+} = D^{+-} = D^{++}$, and that the curl implied by the interior faces equals the curl interpolated from the exterior faces, $c_z^{00} = C_z^{00}$. Because only three of four divergence conditions are linearly independent, we have a system of four independent linear equations for the four desired interior field values. The solution to the system, in matrix form, is:

$$\bar{\mathbf{b}}_{\mathbf{ext}} = \begin{bmatrix} \bar{b}_x^{--} & \bar{b}_x^{-+} & \bar{b}_x^{+-} & \bar{b}_x^{++} & \bar{b}_y^{--} & \bar{b}_y^{-+} & \bar{b}_y^{+-} & \bar{b}_y^{++} \end{bmatrix}^T$$

$$\bar{\mathbf{B}}_{\mathbf{int}} = \begin{bmatrix} \bar{B}_x^{0-} & \bar{B}_x^{0+} & \bar{B}_y^{-0} & \bar{B}_y^{+0} \end{bmatrix}^T$$

$$[\mathbf{A}] = \frac{1}{4} \begin{bmatrix} 2 & 0 & 2 & 0 & 1 & -1 & -1 & 1 \\ 0 & 2 & 0 & 2 & 1 & -1 & -1 & 1 \\ 1 & -1 & -1 & 1 & 2 & 2 & 0 & 0 \\ 1 & -1 & -1 & 1 & 0 & 0 & 2 & 2 \end{bmatrix}$$

$$\bar{\mathbf{B}}_{\mathbf{int}} = [\mathbf{A}]\bar{\mathbf{b}}_{\mathbf{ext}}. \tag{52}$$

In three dimensions, we follow the same procedure to derive the solution for twelve interior refined cell face fields from 24 exterior refined cell face fields. In particular we have eight equations (seven linearly independent) for the volume integrated divergence over each of eight refined cell interiors, $d^{000} = D^{---} = D^{--+} = D^{-+-} = D^{-++} = D^{+--} = D^{+-+} = D^{++-} = D^{+++}$, and six equations (five linearly independent) by computing the three components of the curl, each at two positions relative to the center of the coarse cell, $c_x^{000} = C_x|_{-dx/4} = C_x|_{+dx/4}$, $c_y^{000} = C_y|_{-dy/4} = C_y|_{+dy/4}$, and $c_z^{000} = C_z|_{-dz/4} = C_z|_{+dz/4}$. The solution of this system for the desired interior field values yields the desired prolongation procedure which can be written in the form of equation 52 as:

$$\bar{\mathbf{b}}_{\mathbf{ext}} = \begin{bmatrix} \bar{b}_x^{---} & \bar{b}_x^{--+} & \bar{b}_x^{-+-} & \bar{b}_x^{-++} & \bar{b}_x^{+--} & \bar{b}_x^{+-+} & \bar{b}_x^{++-} & \bar{b}_x^{+++} \\ \bar{b}_y^{---} & \bar{b}_y^{--+} & \bar{b}_y^{-+-} & \bar{b}_y^{-++} & \bar{b}_y^{+--} & \bar{b}_y^{+-+} & \bar{b}_y^{++-} & \bar{b}_y^{+++} \\ \bar{b}_z^{---} & \bar{b}_z^{--+} & \bar{b}_z^{-+-} & \bar{b}_z^{-++} & \bar{b}_z^{+--} & \bar{b}_z^{+-+} & \bar{b}_z^{++-} & \bar{b}_z^{+++} \end{bmatrix}^T$$

$$\bar{\mathbf{B}}_{\mathbf{int}} = \begin{bmatrix} \bar{B}_x^{0--} & \bar{B}_x^{0-+} & \bar{B}_x^{0+-} & \bar{B}_x^{0++} & \bar{B}_y^{-0-} & \bar{B}_y^{-0+} \\ \bar{B}_y^{+0-} & \bar{B}_y^{+0+} & \bar{B}_z^{--0} & \bar{B}_z^{-+0} & \bar{B}_z^{+-0} & \bar{B}_z^{++0} \end{bmatrix}^T$$

$$
[\mathbf{A}] = \frac{1}{16}
\begin{bmatrix}
8 & 0 & 0 & 0 & 8 & 0 & 0 & 0 & 3 & 1 & -3 & -1 & -3 & -1 & 3 & 1 & 3 & -3 & 1 & -1 & -3 & 3 & -1 & 1 \\
0 & 8 & 0 & 0 & 0 & 8 & 0 & 0 & 1 & 3 & -1 & -3 & -1 & -3 & 1 & 3 & 3 & -3 & 1 & -1 & -3 & 3 & -1 & 1 \\
0 & 0 & 8 & 0 & 0 & 0 & 8 & 0 & 3 & 1 & -3 & -1 & -3 & -1 & 3 & 1 & 1 & -1 & 3 & -3 & -1 & 1 & -3 & 3 \\
0 & 0 & 0 & 8 & 0 & 0 & 0 & 8 & 1 & 3 & -1 & -3 & -1 & -3 & 1 & 3 & 1 & -1 & 3 & -3 & -1 & 1 & -3 & 3 \\
3 & 1 & -3 & -1 & -3 & -1 & 3 & 1 & 8 & 0 & 8 & 0 & 0 & 0 & 0 & 0 & 3 & -3 & -3 & 3 & 1 & -1 & -1 & 1 \\
1 & 3 & -1 & -3 & -1 & -3 & 1 & 3 & 0 & 8 & 0 & 8 & 0 & 0 & 0 & 0 & 3 & -3 & -3 & 3 & 1 & -1 & -1 & 1 \\
3 & 1 & -3 & -1 & -3 & -1 & 3 & 1 & 0 & 0 & 0 & 0 & 8 & 0 & 8 & 0 & 1 & -1 & -1 & 1 & 3 & -3 & -3 & 3 \\
1 & 3 & -1 & -3 & -1 & -3 & 1 & 3 & 0 & 0 & 0 & 0 & 0 & 8 & 0 & 8 & 1 & -1 & -1 & 1 & 3 & -3 & -3 & 3 \\
3 & -3 & 1 & -1 & -3 & 3 & -1 & 1 & 3 & -3 & -3 & 3 & 1 & -1 & -1 & 1 & 8 & 8 & 0 & 0 & 0 & 0 & 0 & 0 \\
1 & -1 & 3 & -3 & -1 & 1 & -3 & 3 & 3 & -3 & -3 & 3 & 1 & -1 & -1 & 1 & 0 & 0 & 8 & 8 & 0 & 0 & 0 & 0 \\
3 & -3 & 1 & -1 & -3 & 3 & -1 & 1 & 1 & -1 & -1 & 1 & 3 & -3 & -3 & 3 & 0 & 0 & 0 & 0 & 8 & 8 & 0 & 0 \\
1 & -1 & 3 & -3 & -1 & 1 & -3 & 3 & 1 & -1 & -1 & 1 & 3 & -3 & -3 & 3 & 0 & 0 & 0 & 0 & 0 & 0 & 8 & 8
\end{bmatrix}
\tag{53}
$$

5. Numerical Tests, Examples & Discussion

The AstroBEAR numerical schemes have been tested against a suite of test problems, including the one dimensional tests of Ryu & Jones (1995) and the two dimensional tests of Ryu et al. (1995). Except for the failure of the original Marquina flux formulation to converge for problems involving compound MHD wave structures as discussed in §2.2, each of the methods recover results that are equivalent to those of earlier researchers barring minor differences due to different levels of numerical truncation error. In the remainder of this section we present the results of some of these tests. The results of a few popular hydrodynamic shocktubes are presented which illustrate the differences between and limitations of each of the reconstruction and upwinding methods. In these cases we provide commentary which is intended to provide guidance as to the optimal choice of methods given the expected physical regime of a particular simulation. We also reproduce the results of several of the two dimensional tests of Ryu et al. (1995) using AMR. These tests demonstrate the success of the divergence preserving restriction and prolongation operators presented in §4.

5.1. One Dimension

Figure 8 shows the density resulting from the Sod (1978) shock tube problem denoted as "test problem 1" in the book by Toro (1999) using several spatial reconstruction methods. The initial left and right Riemann problem states, number of computational zones and final time of the solution are presented in table 2. In all three cases the Runge-Kutta temporal integration and the flux formulation of Roe was used. We note that the result of this test

is not very sensitive to the choice of temporal reconstruction method or flux formulations. The shock tube consists from left to right of a backward propagating rarefaction, a contact discontinuity, and a forward propagating shock wave. The numerical diffusion caused by the truncation error of each of the spatial reconstruction methods is readily apparent in the figure. We characterize the diffusion of the method by the width of the contact discontinuity. The three methods are presented in order of increasing diffusion. The least diffusive method, PPM resolves the contact across three zones, and the most diffusive method, MUSCL resolves the contact across 8 zones. We note that the diffusion of the PPM and MUSCL methods may be improved by choosing a more compressive slope limiter than the MINMOD limiter used here at the expense of introducing oscillations near sharp discontinuities in the flow. Naturally, those methods which exhibit the least numerical diffusion are the most accurate. However, the PPM and PHM methods tend to "overshoot" the solution near sharp discontinuities, thereby introducing small oscillations into the solution. Such oscillations may drive numerical pathologies in simulations of flow with very low pressure near discontinuities such as persistently negative pressures. We note that some researchers have managed to reduce such oscillations by introducing additional sources of diffusion to the base scheme (see, for example §B1 of Mignone et al. (2005)). Simulation of astrophysical phenomena involving strong radiative cooling is particularly susceptible to this problem. In such cases the optimal solution strategy is determined as a trade-off between the desire for simultaneously low numerical diffusion and low oscillation.
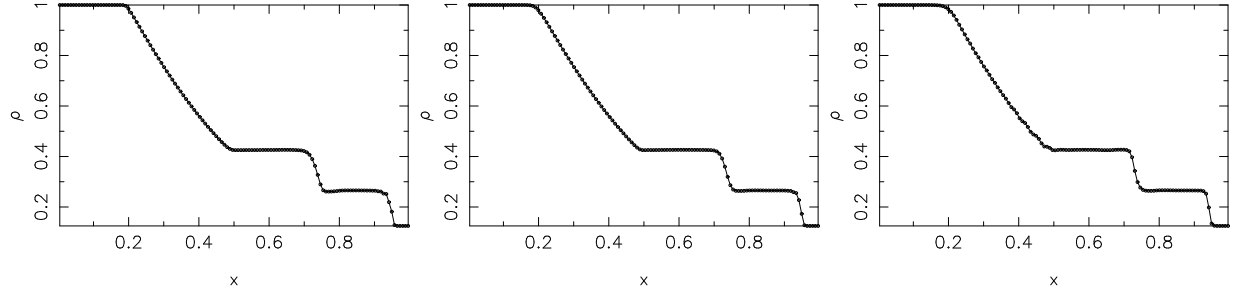
Fig. 8.— Result of the Sod (1978) shocktube (test problem 1 of Toro (1999)) using MUSCL/VL slope limiter (left), PHM (center) and PPM (right) spatial reconstruction.

Table 2: Sod Shocktube Parameters.

	left, $x < 0.5$	right, $x \geq 0.5$
ρ	1	0.125
v_x	0	0
P	1	0.1
γ	1.4	1.4
grid zones	128	
CFL	0.9 (0.5 for PPM)	
t_{final}	0.25	

Figure 9 shows the result of the "1-2-0-3" strong expansion shock tube of Einfeldt et al. (1991), denoted as "test problem 2" in the book by Toro (1999). The initial left and right Riemann problem states, number of computational zones and final time of the solution is presented in table 3. This shock tube launches two rarefaction waves, one propagating to the left and one propagating to the right. The upper three panels show the test results utilizing the MUSCL - VL slope spatial and Ruge-Kutta temporal reconstruction methods with different flux upwinding procedures. This test problem was designed to illustrate the failure mode common to linearized Riemann solvers evident by the anomalous oscillation in velocity and anomalous rise in specific thermal energy(E_{th}/ρ) about the center of the grid in panel 9a. These anomalies are caused by the addition of small amounts of thermal energy to the solution in regions where the pressure becomes negative. We note that specific thermal energy anomalies such as these can result in a cascade of numerical pathologies in multi-physics simulations involving temperature dependent micro-physics. Einfeldt et al. (1991) showed that the more diffusive HLLE Riemann solver, under certain conditions, guarantees pressure positivity and therefore reduces such anomalies. Gardiner & Stone (2005) have also demonstrated success applying the HLLE solver only in those regions where the linearized solver produces negative pressure or density. In panel 9b we show that application of the Marquina flux formulation also resolves the anomalous behavior. In §2.2 we presented an adaptation of the Marquina flux formulation which is better suited to magnetized flow involving compound wave structures. The result of this calculation utilizing the adapted flux formulation (panel 9c) shows that the adaptation retains the desirable features of the Marquina flux for this test problem.
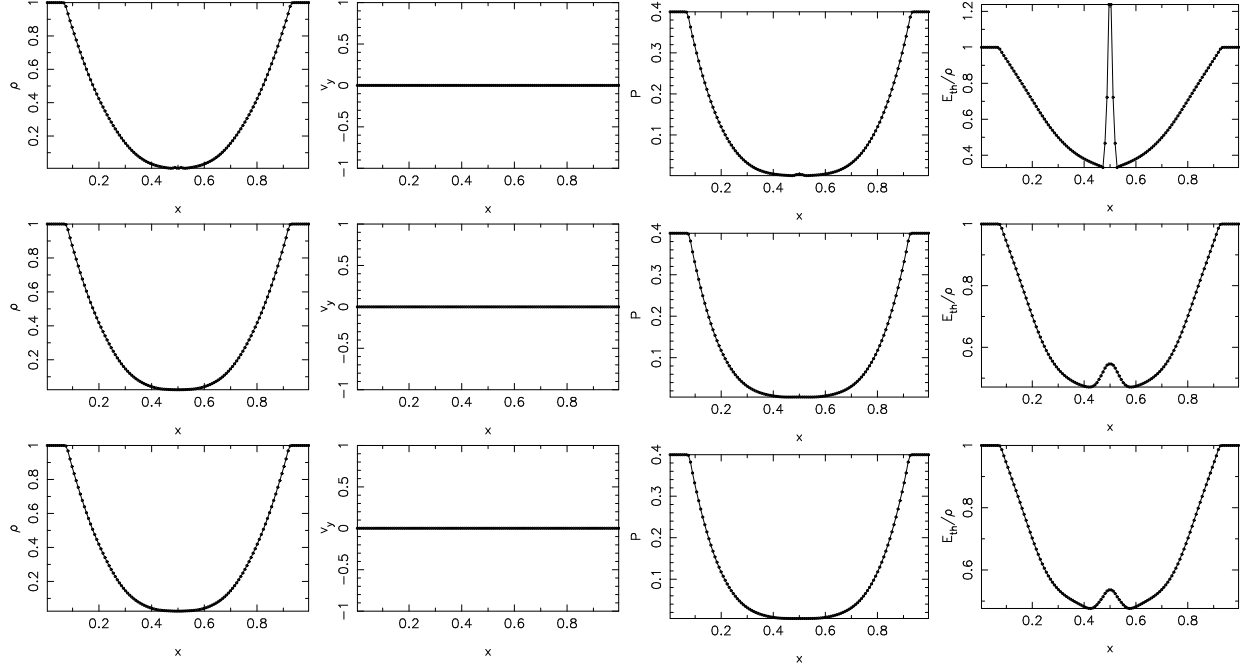
Fig. 9.— Results of the Einfeldt et al. (1991) "1-2-0-3" strong rarefaction shocktube (test problem 2 of Toro (1999)) using the Roe flux, the Marquina flux, and the adapted Marquina flux from top to bottom.

Table 3: Einfeldt Shocktube Parameters.

	left, $x < 0.5$	right, $x \geq 0.5$
ρ	1	1
v_x	-2	2
P	0.4	0.4
γ	1.4	1.4
grid zones	128	
CFL	0.8	
t_{final}	0.15	

In figure 9 we reproduce the MHD shock tube test from figure 2a of Ryu & Jones (1995). Following the notation of Ryu & Jones (1995), we denote the orientation angle of the magnetic field, $\Psi = \tan^{-1}(B_z/B_y)$. The initial left and right Riemann problem states, number of computational zones and final time of the solution is presented in table 3. This Riemann problem demonstrates the ability of the code to correctly capture a number of MHD discontinuities. The discontinuities in the flow from left to right are, (1) fast shock, (2) rotational discontinuity, (3) slow shock, (4) contact discontinuity, (5) slow shock, (6) rotational discontinuity, and (7) fast shock. We note that the PHM spatial reconstruction employed for this test generally results in a level of truncation error slightly lower than that of Ryu & Jones (1995) with a slightly more diffusive result about of rotational discontinuities due to the lack of a rotational discontinuity steepening procedure like that of equations 2.96 - 2.98 of Ryu & Jones (1995). We note that when applied to this particular problem, the MUSCL and PPM spatial reconstruction methods result in lower and higher truncation error respectively, in a manner that is similar to Sod problem discussed earlier.
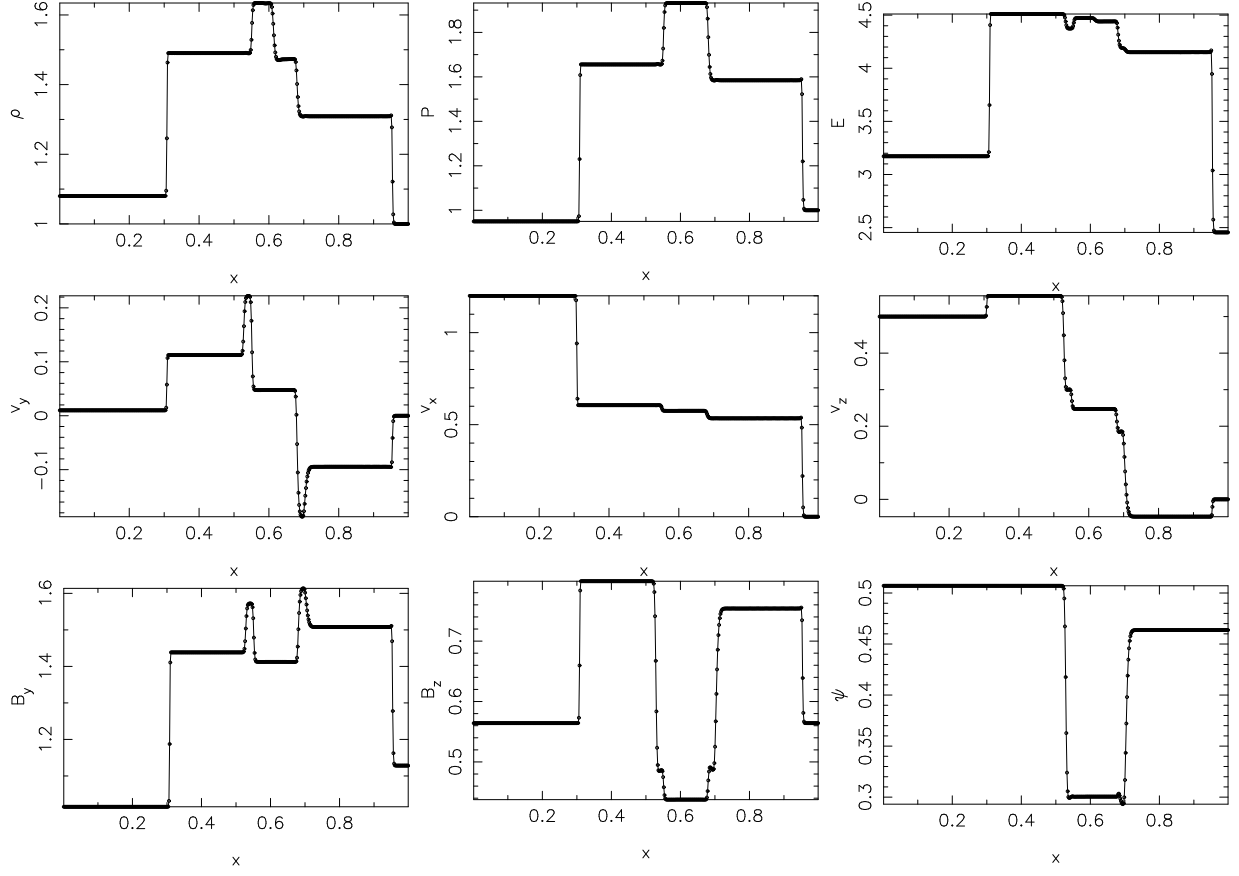
Fig. 10.— MHD shocktube result using PHM spatial reconstruction, MUSCL-Hancock temporal reconstruction, and the Roe flux function.

Table 4: MHD Shocktube Parameters.

	left, $x < 0.5$	right, $x \geq 0.5$
ρ	1.08	1
v_x	1.2	0
v_y	0.01	0
v_z	0.5	0
P	0.95	1
B_x	$2/\sqrt{4\pi}$	$2/\sqrt{4\pi}$
B_y	$3.6/\sqrt{4\pi}$	$4/\sqrt{4\pi}$
B_z	$2/\sqrt{4\pi}$	$2/\sqrt{4\pi}$
γ	5/3	5/3
grid zones	512	
CFL	0.8	
t_{final}	0.2	

5.2. Two Dimensions

In this section we present the results of several two dimensional simulations to demonstrate the robustness of the divergence preserving scheme in AMR applications. The simulations presented in this section which utilize the AMR functionality of the code apply an AMR hierarchy of 3 levels using a refinement ratio of 2 between levels.

We begin with the problem of the advection of a weak magnetic field loop following the prescription given in Gardiner & Stone (2005) and Gardiner & Stone (2008). The initial conditions given in table 5. The initial face-centered magnetic field is generated from the analytic prescription of the vector potential ($\mathbf{B} = \nabla \times \mathbf{A}$) at cell corners using a centered difference formula on a grid extending from $0 \leq L_x \leq 2$, $0 \leq L_y \leq 1$ with resolution $2N \times N$. In the left column figure 11 we show magnetic field lines (red) over a greyscale representation of the current density $\mathbf{J} = \nabla \times \mathbf{B}$ for the initial condition (top) and after the advection of the loop through the periodic domain at $t = 1$ for both the Runge-Kutta (center) and MUSCL-Hancock temporal integration (bottom) with a resolution of $N = 128$. In both cases monotized-center limited linear spatial reconstruction with the flux function of Roe were used. The problem contains an initially singular current sheet along the surface and a singular spike at the center which is very sensitive to error in the evolution of the magnetic field. The propagation of these singular features through the grid serves as a very stringent test of the MHD update algorithm. We find that both methods maintain the correct location of these singularities and maintain magnetic field contours that are smooth and nearly symmetric about the current spike.

The top and center portions of the right column of figure 11 show the evolution of the spatially averaged magnetic energy normalized to the initial analytic value B_o for the MUSCL-Hancock and Runge-Kutta integration approaches respectively for different grid resolutions. We find that both methods show comparable accuracy and the expected convergence properties for this quantity. However, the direction split MUSCL-Hancock scheme shows inexact evolution of the axial component of the magnetic field B_z and that this error converges slowly as shown in the lower right panel of figure 11 whereas the unsplit Runge-Kutta scheme maintains $B_z = 0$ exactly to machine precision. This error is due to the failure of the direction split scheme to produce the an exactly divergence free representation of the magnetic field for the time-centered predictor state as discussed in the last paragraph of §2.4. In particular, as noted by Gardiner & Stone (2008), the evolution of the z-component of the magnetic induction equation reduces to $\partial B_z/\partial t = v_z(\partial B_x/\partial x + \partial B_y/\partial y)$ so that with finite v_z the exact evolution of B_z will only be maintained for unsplit schemes with exactly divergence free reconstruction.
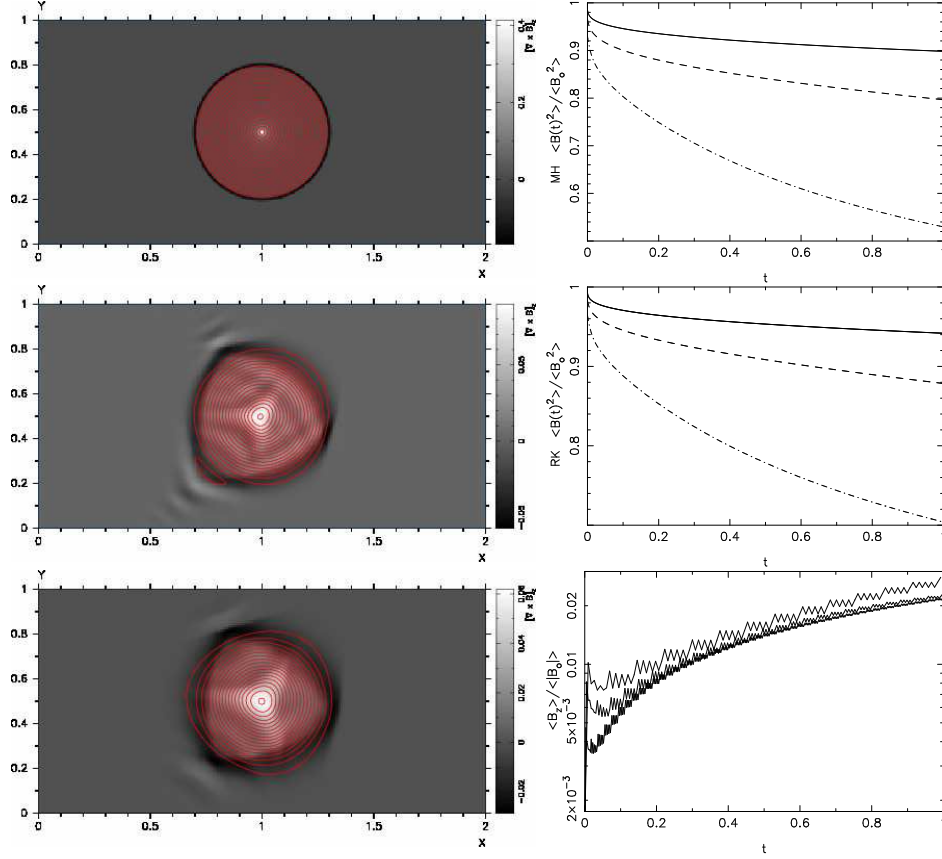
Fig. 11.— Left: Field loop advection magnetic field lines (red) over a greyscale representation of the current density $\mathbf{J} = \nabla \times \mathbf{B}$ for the initial condition (top) and after the advection of the loop through the periodic domain at $t = 1$ for both the Runge-Kutta (center) and MUSCL-Hancock temporal integration (bottom). Right: Evolution of the spatially averaged magnetic energy normalized to the initial analytic value B_o for the MUSCL-Hancock (top) and Runge-Kutta (center) integration. The grid resolutions shown correspond to $N = 32, 64$ and 128 for the dash-dot, dash and solid lines respectively. Evolution of the spatial average of the normalized axial component of the magnetic field $|B_z|$ for the direction split MUSCL-Hancock integrator (bottom). The plot shows decreasing error for the three resolutions $N = 32, 64$ and 128.

Table 5: MHD Loop Advection Parameters.

ρ	1
v_x	2
v_y	1
v_z	1
P	1
A_z	$B_o(r - R)$ if $r \leq R$
	0 otherwise
r	$\sqrt{(x-1)^2 + (y-1)^2}$
B_o	10^{-3}
R	0.3
γ	5/3
CFL	0.9 (MUSCL-Hancock)
	0.45 (Runge Kutta)

The next set of simulations show the propagation of a cylindrical, supersonic cloud through a magnetized medium where the magnetic field is oriented parallel to the propagation of the cloud (figure 12, top), perpendicular to the propagation of the cloud (figure 13, middle), and 45° to the propagation of the cloud (figure 13, bottom). These simulations have been carried out using PHM spatial reconstruction, MUSCL-Hancock temporal reconstruction, the adapted Marquina flux and the constrained transport evolution of the magnetic field of Ryu et al. (1995). Each of these simulations employ constant extrapolation conditions along each boundary. The AMR level with the finest resolution achieves an effective resolution of 32 cells per cloud radius. The initial cloud density is smoothed linearly to that of the ambient environment and the velocity is smoothed over the outer four computational cells of the cloud. The figures show the result of each simulation at two evolutionary times, $t = 2t_{cr}$ in the left panel and $t = 4t_{cr}$ in the right panel where $t_{cr} = 2r_c\sqrt{\chi}/v_c$ is the cloud crushing time where r_c is the cloud radius, v_c is the initial cloud speed and χ is the density contrast of the cloud against the ambient environment (see Jones et al. (1996) for details). The density distribution is presented in gray-scale, red lines delineate the magnetic field lines and blue lines delineate regions of AMR-enhanced resolution. We note that the turbulent wake behind the 45° cloud and the associated early onset of tearing mode instability and magnetic reconnection pose some degree of numerical difficulty which requires the use of the more accurate and robust Runge-Kutta method over the faster MUSCL-Hancock method. The simulations use the same initial physical parameters as the simulations presented in Ryu et al. (1998) and Jones et al. (1996) which are presented in table 5.

Because the shocked cloud simulations presented here do not utilize a moving mesh, the final time ($t = 4t_{bc}$) of the simulations is somewhat earlier than that of the earlier works ($t = 6t_{bc}$) of Ryu et al. (1995) and Jones et al. (1996). The density distribution and magnetic field lines at ($t = 2t_{bc}$) show agreement with results of the earlier calculations at the same evolutionary time. As pointed out in Ryu et al. (1995) and Jones et al. (1996), the nonlinear evolution of the cloud depends sensitively on the exact initial perturbations which develop out of the geometric mismatches between the cloud and the computational grid. The agreement of the AMR simulations presented here with the earlier works demonstrates the robustness and accuracy of the divergence preserving restriction and prolongation procedures presented in §4.
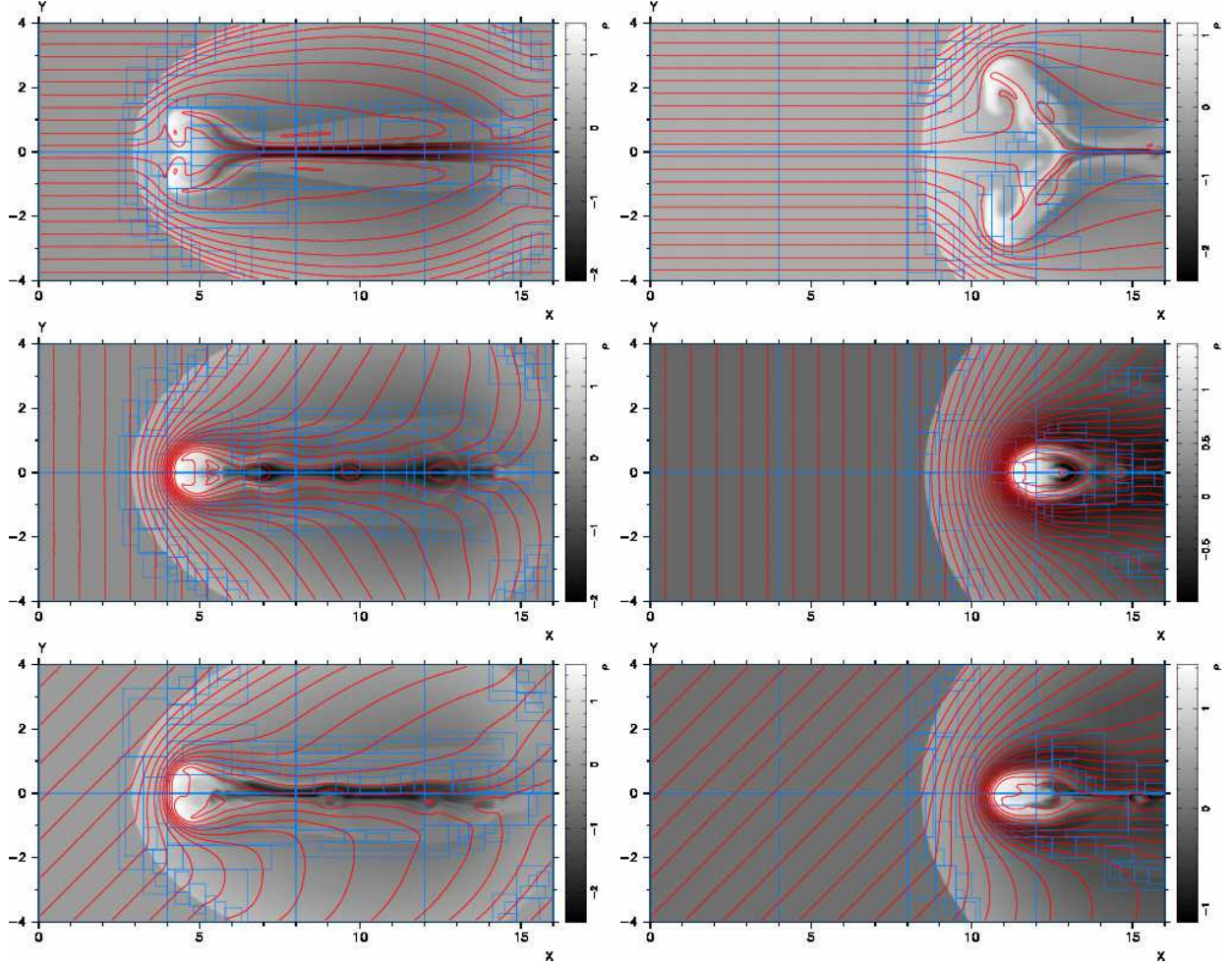
Fig. 12.— Simulation results of a supersonic cylindrical cloud moving through a magnetized medium with initial magnetic field oriented parallel, perpendicular and diagonal to the propagation of the cloud from top to bottom. The logarithm of the density distribution is presented in gray-scale, red lines delineate the magnetic field lines and blue lines delineate regions of AMR-enhanced resolution.

Table 6: MHD Shocked Cloud Parameters.

	ambient	cloud
ρ	1	10
v_x	10	0
v_y	0	0
v_z	0	0
P	$1/\gamma$	$1/\gamma$
β	4	4
γ	5/3	5/3
clump radius (r_c)	1	
grid zones per cloud radius	32	
initial cloud position	(2, 0)	
CFL	0.4	

In figure 13 we reproduce the light cylindrical MHD jet simulation of Ryu et al. (1995) and Lind et al. (1989). A jet with a top-hat profile is injected into a uniformly magnetized environment by imposing the physical jet conditions presented in table 7 inside of $r \leq r_j$ along the $z = 0$ boundary. The symmetry of the problem dictates the use of reflecting boundary conditions along the $r = 0$ boundary. All other boundaries utilize constant extrapolation. The simulation was carried forward on an AMR hierarchy with four levels of refinement utilizing the PHM spatial integration method with Runge-Kutta temporal integration, the Roe flux upwinding method, and the constrained transport magnetic field evolution of Ryu et al. (1998). The finest AMR level has a resolution of 32 cells per jet radius. The figures show the result of the simulation at 5 evolutionary times, $t = 2.43$, 6.57, 10.62, 14.76, and 18.00. Note these are the same evolutionary times shown in the results of Ryu et al. (1998) scaled to the dimensionless units defined by the parameters listed in 7. The density distribution is presented in gray-scale, red lines delineate the magnetic field lines and blue lines delineate regions of AMR-enhanced resolution. Because the simulations were carried out in cylindrical symmetry, the lower half of each panel has been plotted by reflecting the computational domain about the symmetry axis. Barring differences in the detail of the nonlinear evolution of the Kelvin-Helmholtz shear flow behind the jet bow shock which arise from the exact nature of the numerical perturbations present in the simulation, the simulation results show excellent agreement with that of Ryu et al. (1995) at each evolutionary stage shown in the panels of figure 13. The agreement of the AMR simulations presented here with the earlier works demonstrates the robustness and accuracy of the divergence preserving restriction and prolongation procedures presented in §4 and the adaptations thereof for cylindrical geometry presented in the appendix.
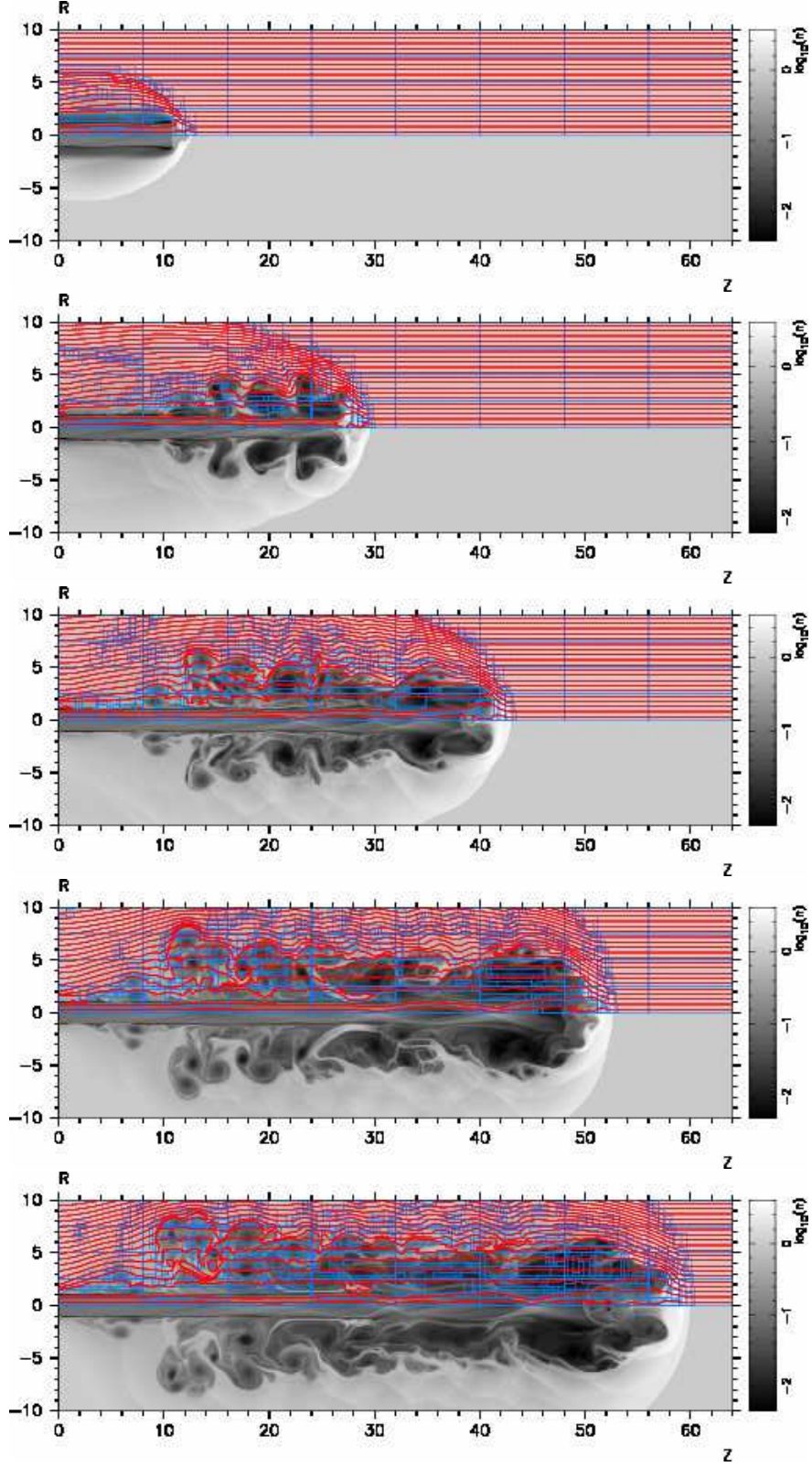
Fig. 13.— Light MHD jet simulation. The logarithm of the density distribution is presented in gray-scale, red lines delineate the magnetic field lines and blue lines delineate regions of AMR-enhanced resolution at $t = 2.43$, 6.57, 10.62, 14.76, and 18.00 from top to bottom.

Table 7: Light MHD Jet Parameters.

	ambient	jet
ρ	0.1	1
v_x	0	20
v_y	0	0
v_z	0	0
P	$1/\gamma$	$1/\gamma$
B_r	0	0
$B_\theta(r)$	0	$2\sqrt{0.02/\gamma}\ r/r_j$
B_z	$\sqrt{0.02/\gamma}$	$\sqrt{0.02/\gamma}$
γ	5/3	5/3
jet radius r_j	1	
grid zones per jet radius	32	
CFL	0.4	

To confirm the robustness of the code and to demonstrate its application with radiative energy loss, we illustrate the propagation of a strongly radiative shock through an inhomogeneous environment. The inhomogeneities in these two dimensional calculations take the form of a random distribution of 150 cylindrical clouds with 100 times the density of the ambient environment at their center. The density of the clouds follow a hyperbolic tangent smoothing function to the ambient density along the outer 50% of the radius of each cloud. The inhomogeneities are initially in pressure balance with the ambient environment. The upper and lower boundaries of the computational domain are periodic, the right boundary follows a constant extrapolation and the wind state is held constant in the left boundary throughout the simulation. The physical state of the ambient environment, the center of the clouds, and the ambient environment are given in table 8. Figures 14 and 15 show the results of the simulations at several evolutionary stages ($t = 0$, 92, 184 and 369 yr). The simulations were carried forward using MUSCL spatial reconstruction, Runge-Kutta temporal integration, the adapted Marquina flux upwinding and the constrained transport method of Ryu et al. (1995). An operator split energy sink source term is used to include the effects of radiative energy loss via atomic line cooling using the cooling function of Dalgarno & McCray (1972). The density distribution is presented in gray-scale, red lines delineate the magnetic field lines and blue lines delineate regions of AMR-enhanced resolution. Figure 14 shows the case where the magnetic field oriented parallel to the direction of wind and figure 15 shows the case where the ambient environment is threaded with a magnetic field that is oriented perpendicular to the direction of an unmagnetized wind. The turbulent nature of the flow pattern that emerges in simulations, compounded sock compression ratios as high as ~ 12 which are achieved via radiative losses results in the development of persistently converging flow. Such flows are particularly problematic for codes that do not maintain the solenoidal constraint on the magnetic field as local divergences tend to accumulate in highly compressed regions of the flow (Balsara & Kim 2004). These simulations, therefore, demonstrate the robustness of the methods described in this paper for the simulation of such flows.
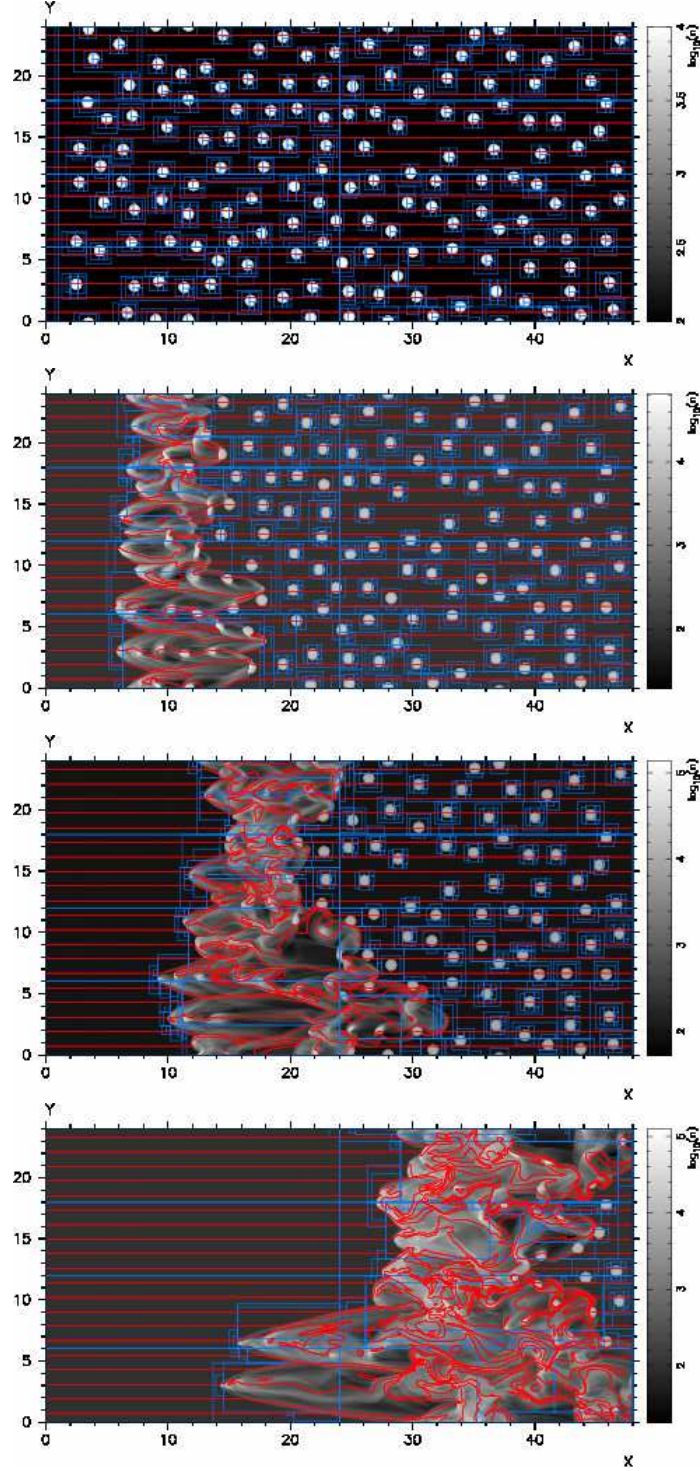
Fig. 14.— Shock propagation through multiple clouds with magnetic field oriented parallel to the direction of shock propagation at evolutionary time $t = 0$, 92, 184 and 369 yr. The logarithm of the density distribution in cm^{-3} is presented in gray-scale, red lines delineate the magnetic field lines, blue lines delineate regions of AMR-enhanced resolution and the cloud diameter is used as the length unit.
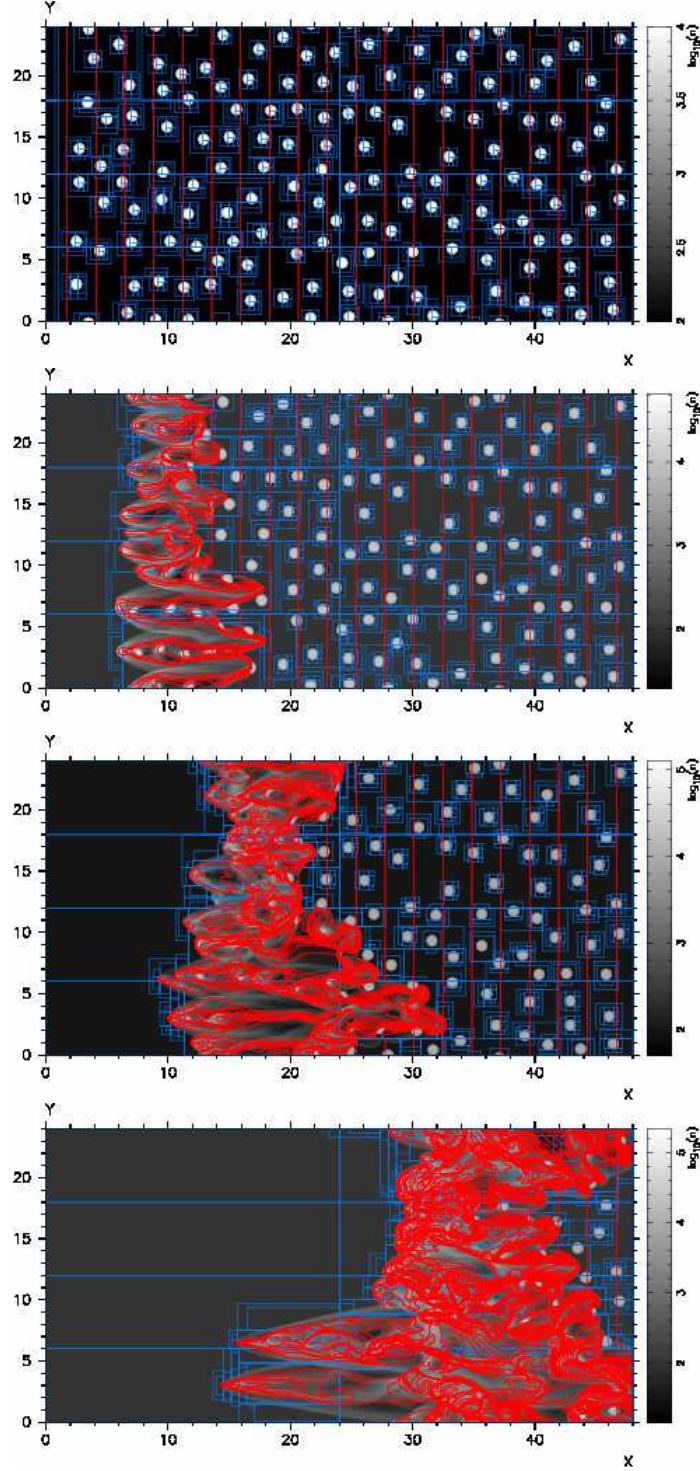
Fig. 15.— Shock propagation through multiple clouds with magnetic field oriented perpendicular to the direction of shock propagation at evolutionary time $t = 0$, 92, 184 and 369 yr. The logarithm of the density distribution in cm^{-3} is presented in gray-scale, red lines delineate the magnetic field lines, blue lines delineate regions of AMR-enhanced resolution and the cloud diameter is used as the length unit.

Table 8: Multiple Cloud Parameters.

	ambient	cloud	wind
$\rho \ (cm^{-3})$	100	10^4	100
$v_x \ (km s^{-1})$	0	0	150
v_y	0	0	0
v_z	0	0	0
$T \ (k)$	200	0.2	10^4
γ	5/3	5/3	5/3
cloud radius (AU)	50		
grid zones per cloud radius	12		
CFL	0.4		

5.3. Three Dimensions

Circularly polarized Alfven waves are an exact nonlinear solution to the MHD equations. We follow an approach similar to that of Gardiner & Stone (2008) and Tóth (2000) by rotating the one dimensional prescription of the problem (table 9) onto a three dimensional periodic grid of size $\sqrt{6}/2 \times \sqrt{6} \times \sqrt{6}$ with resolution $N \times 2N \times 2N$ via the rotation:

$$
\begin{bmatrix} x \\ y \\ z \end{bmatrix} = \begin{bmatrix} \cos(\alpha)\cos(\beta) & -\sin(\alpha) & -\cos(\alpha)\sin(\beta) \\ \sin(\alpha)\cos(\beta) & \cos(\alpha) & -\sin(\alpha)\sin(\beta) \\ \sin(\beta) & 0 & \cos(\beta) \end{bmatrix} \begin{bmatrix} x_1 \\ y_1 \\ z_1 \end{bmatrix} \tag{54}
$$

where $\alpha = \arcsin(1/\sqrt{5})$ and $\beta = \arcsin(1/\sqrt{6})$ so that the initial state is periodic with the grid and the wave-vector points along the diagonal of the computational domain. Solutions have been computed for one crossing time ($t = 1$) using monotonized-centered limited linear spatial reconstruction, the Roe flux function and both the unsplit Runge-Kutta and direction split MUSCL-Hancock temporal integrators. The left panel figure 16 shows the convergence of the volume averaged norm of the L_1 error vector as measured with respect to the initial state

$$
\epsilon = \frac{1}{4N^3} \sqrt{\sum_{nq} \left(\sum_{i,j,k} |q_{i,j,k,nq}^{t=1} - q_{i,j,k,nq}^{t=0}| \right)^2} \tag{55}
$$

for grid resolutions of $N = 8, 16, 32$ and 64. Consistent with the results of other authors on this test problem (Tóth 2000; Gardiner & Stone 2005, 2008), the solution error arises mainly from the magnetic field components that are transverse to the wave propagation direction. The right panel of figure 16 shows the steady convergence of the amplitude of the transverse components of the magnetic $B_T = \sqrt{B_{y1}^2 + B_{z1}^2}$ field after rotating back into the unrotated space

$$
\begin{bmatrix} x_1 \\ y_1 \\ z_1 \end{bmatrix} = \begin{bmatrix} \cos(\alpha)\cos(\beta) & \sin(\alpha)\cos(\beta) & \sin(\beta) \\ -\sin(\alpha) & \cos(\alpha) & 0 \\ -\cos(\alpha)\sin(\beta) & -\sin(\alpha)\sin(\beta) & \cos(\beta) \end{bmatrix} \begin{bmatrix} x \\ y \\ z \end{bmatrix} \tag{56}
$$

for the unsplit Runge-Kutta case. Both integration techniques converge in a manner consistent with the expected second order accuracy with least squared power-law induces $\epsilon \propto N^{-1.92}$ for the MUSCL-Hancock scheme and $\epsilon \propto N^{-2.49}$ for the Runge-Kutta scheme.
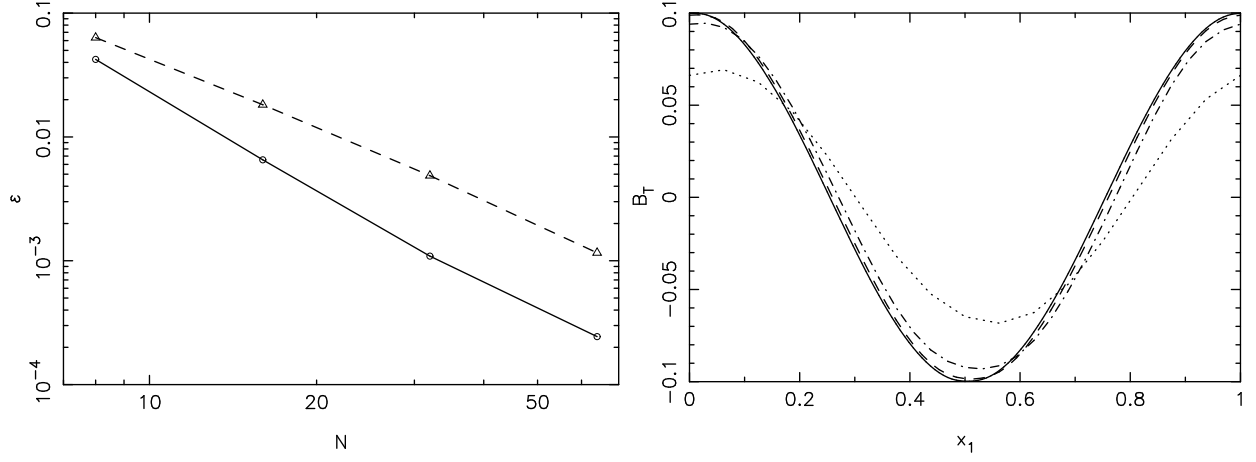
Fig. 16.— Circularly polarized Alfven wave in three dimensions: Left: convergence of the L_1 error for the direction split MUSCL-Hancock temporal reconstruction (dotted) and the unsplit Runge Kutta temporal reconstruction (solid), Right: transverse component of the magnetic field (right) after one grid crossing ($t = 1$) for grid resolutions $N = 8$ (dot) , 16 (dash-dot , 32 (dash) and 64 (solid) .

Table 9: Circularly Polarized Alfven Wave Parameters.

ρ	1
v_1	0
v_2	$a\sin(2\pi x_1)$
v_3	$a\cos(2\pi x_1)$
P	1
B_1	1
B_2	$a\sin(2\pi x_1)$
B_3	$a\cos(2\pi x_1)$
a	0.1
R	0.3
γ	5/3
Δt	$1/(3N)$ (MUSCL-Hancock)
	$1/(6N)$ (Runge Kutta)

6. Conclusion

The staggered grid constrained transport schemes described in this paper enable the application of high resolution shock capturing methods to magnetized flow. In this paper we have demonstrated that a wide cross section of high resolution shock capturing schemes for general conservation laws may be adapted for magnetized flow while preserving the divergence free constraint on the magnetic field topology exactly by conserving the surface integral of magnetic flux over each computational cell in an upwind fashion. The use of such schemes on multi-resolution AMR grids is encumbered by the requirement that the prolongation and restriction steps preserve the divergence free topology of the magnetic fields. In this paper we have described the application of prolongation and restriction operators which maintain such topologies to machine precision.

The numerical schemes discussed here have been implemented and tested in the AstroBEAR adaptive mesh refinement code. The code utilizes a modular design, enabling the user to choose from various methodologies to tailor the numerical integration strategy to the requirements of the application at hand. The robustness of this approach to high resolution, shock capturing MHD on AMR grid structures, and relative advantages of the various numerical schemes implemented in the code are demonstrated in the context of several numerical example problems. The description of the numerical schemes presented in this paper provides a concise recipe for their implementation which will enable the reproduction of these outcomes by other researchers and the interpretation of future works derived from the AstroBEAR code.

A. Cylindrical Axisymmetry

The conservative update procedure for integrating the ideal MHD equations §2 may be readily extended to the case cylindrical axisymmetric flows via a change in the coordinate variables and the addition of a source term to equation 2. In particular, the coordinate subscripts transform as as $(x, y, z), \rightarrow (r, \theta, z)$ and the source term becomes:

$$\mathbf{S} = -\frac{1}{r} \ [\rho v_r, \rho v_r^2 - B_r^2 + B_\theta - \rho v_\theta^2, 2(\rho v_r v_\theta - B_\theta B_r), \rho v_r v_z - B_z B_r,$$
$$v_r(E + P + \mathbf{B}^2/2) - B_r(\mathbf{B} \cdot \mathbf{v}), 0, 0, v_r B_z - v_z B_r]^T. \tag{A1}$$

Due to axisymmetry, all differential terms in θ vanish. We handle the geometric source term, $\mathbf{S}$ separately from the conservative update of the homogeneous part of the system using an operator split approach. The source term step $\frac{\partial \mathbf{Q}}{\partial t} = \mathbf{S}$ is integrated via a fourth-order Rosenbrock integration scheme for stiff systems of ordinary differential equations (Press et al. 1992) using an adaptive time-step to maintain the accuracy of the solution to a user specified level (usually 1 part in 10^4). Symmetry dictates that such simulations be carried out in a half-meridional plane $(r \geq 0)$ and that reflecting boundary conditions be applied along the $r = 0$ plane.

The constrained transport of §2.4 and prolongation / restriction of §4 of grid-interface magnetic field components, B_r and B_z may also be readily adapted for cylindrical axisymmetric flow. Readers interested in the extention to more complicated geometries may refer to the work of Balsara (2004) which derives divegence free reconstruction procedures in several three dimensional curvilinear geometries and on tetrahedral meshes. In cylindrical axisymmetry, the solenoidality constraint on the magnetic field takes the form:

$$\nabla \cdot \mathbf{B} = \frac{1}{r}\frac{\partial r B_r}{\partial r} + \frac{\partial B_z}{\partial z} = 0, \tag{A2}$$

and the component of the curl of the magnetic field orthogonal to the symmetry plane takes the form:

$$[\nabla \times \mathbf{B}]_\theta = \frac{\partial B_r}{\partial z} - \frac{\partial B_z}{\partial r}. \tag{A3}$$

These operators take the same form as the Cartesian case under the change of variable $B_r \rightarrow r B_r$. Therefore CT update formulae of §2.4 and the prolongation and restriction forulae of §4 are written for the case of axisymmetry by replacing $(\tilde{f}_x, \tilde{f}_z) \rightarrow (\tilde{f}_r, \tilde{f}_z)$, $E_y \rightarrow E_\theta$, $(B_x, B_z) \rightarrow (r B_r, B_z)$, and $(b_x, b_z) \rightarrow (r b_r, b_z)$. The CT integration procedure (equations 31) can be written for axisymmetric geometry by replacing $B_z \rightarrow r B_z$ and $E_y \rightarrow r E_\theta$.

B. Pseudo-code listing for the AMR engine.

```
SUBROUTINE AMR(level, dt)
  IF(level=0)
    nsteps = 1
    Set Ghost(level)
  ELSE
    nsteps = r
  END IF
  DO n = 1, nsteps
    Distribute(level)
    IF(level < MaxLevel)
       Grid Adapt(level + 1)
       Set Ghost(level+1)
    END IF
    Integrate(level,n)
    IF(level< MaxLevel)  AMR(level + 1, dt/r)
  END DO
  IF(level > 1) Syncronize to Parent(level)
END SUBROUTINE AMR
```

REFERENCES

Balsara, D. S. 1998, ApJS, 116, 119

Balsara, D. S. 1998, ApJS, 116, 133

Balsara, D. S. 2001, J. Comput. Phys., 174, 614

Balsara, D. S. 2004, ApJS, 151, 149

Balsara, D. S., & Kim, J. 2004, ApJ, 602, 1079

Balsara, D. S., & Spicer, D. S. 1999, J. Comput. Phys., 149, 270

Brackbill, J. U., & Barnes, D. C. 1980, J. Comput. Phys., 35, 426

Brio, M., & Wu, C. C. 1988, J. Comput. Phys., 75, 400

Berger, M. J., & Colella, P. 1989, J. Comput. Phys., 82, 64

Berger, M. J., & Oliger, J. 1984, J. Comput. Phys., 53, 484

Berger M., & Rigoutsos I., . 1991 IEEE Trans. Systems, Man & Cyber 21:5, 1278

Colella, P. 1990, J. Comput. Phys., 87, 171

Colella, P., & Woodward, P. R. 1984, J. Comput. Phys., 54, 174

Crockett, R. K., Colella, P., Fisher, R. T., Klein, R. I., & McKee, C. F. 2005, J. Comput. Phys., 203, 422

Cunningham, A., Frank, A., & Hartmann, L. 2005, ApJ, 631, 1010

Cunningham, A. J., Frank, A., & Blackman, E. G. 2006, ApJ, 646, 1059

Cunningham, A. J., Frank, A., Quillen, A. C., & Blackman, E. G. 2006, ApJ, 653, 416

Dai, W., & Woodward, P. R. 1998, ApJ, 494, 317

Dalgarno, A. & McCray, R. A. 1972, ARA&A, 10, 375

Dedner, A., Kemm, F., Kröner, D., Munz, C.-D., Schnitzer, T., & Wesenberg, M. 2002, J. Comput. Phys., 175, 645

Dennis, T. J., Cunningham, A. J., Frank, A., Balick, B., Blackman, E. G., & Mitran, S. 2008, ApJ, 679, 1327

Donat, R., & Marquina, A. 1996, J. Comput. Phys., 125, 42

Einfeldt, B.,Munz, C. D., Roe, P. L. & Sjogreen, B. 1991, J. Comput. Phys., 92, 273

Evans, C. R., & Hawley, J. F. 1988, ApJ, 332, 659

Falle, S. A. E. G. 2002, ApJ, 577, L123

Fromang, S., Hennebelle, P., & Teyssier, R. 2006, A&A, 457, 371

Fryxell, B., et al. 2000, ApJS, 131, 273

Gardiner, T. A., & Stone, J. M. 2005, J. Comput. Phys., 205, 509

Gardiner, T. A., & Stone, J. M. 2008, J. Comput. Phys., 227, 4123

Harten, A., Hyman, J. M., & Lax, P. D. 1976, Communications in Pure Applied Mathematics, 29, 297

Jiang, G.-S., & Wu, C.-C. 1999, J. Comput. Phys., 150, 561

Jones, T. W., Ryu, D., & Tregillis, I. L. 1996, ApJ, 473, 365

Keppens R., Nool M., Toth G., Goedbloed, Comput. Phys. Comm., 2003, 153, 317

Khokhlov, A. M. 1998, J. Comput. Phys., 220, 678

Kim, J., Ryu, D., Jones, T. W., & Hong, S. S. 1999, ApJ, 514, 506

Klein, R. I. 1999, J. Comp. Appl. Math., 109, 12

Leveque, R. J., 2002 Finite Volume Methods for Hyperbolic Problems, Cambridge University Press

Li, S., & Li, H. 2004, J. Comput. Phys., 199, 1

Lind, K. R., Payne, D. G., Meier, D. L., & Blandford, R. D. 1989, ApJ, 344, 89

Londrillo, P., & Del Zanna, L. 2000, ApJ, 530, 508

Marquina, A. 1994, SIAM J.Sci.Comput., 15:4, 892

Mignone, A., Bodo, G., Massaglia, S., Matsakos, T., Tesileanu, O., Zanni, C., & Ferrari, A. 2007, ApJS, 170, 228

Mignone, A., Plewa, T., & Bodo, G. 2005, ApJS, 160, 199

Miller, G. H. & Colella, P. 2002, J. Comput. Phys., 183, 26

Miyoshi, T., & Kusano, K. 2005, J. Comput. Phys., 208, 315

O'Shea, B. W., Bryan, G., Bordner, J., Norman, M. L., Abel, T., Harkness, R., & Kritsuk, A. 2004, Adaptive Mesh Refinement - Theory and Applications", Eds. T. Plewa, T. Linde & V. G. Weirs, Springer Lecture Notes in Computational Science and Engineering

Powell, K. G., Roe, P. L., Linde, T. J., Gombosi, T. I., & de Zeeuw, D. L. 1999, J. Comput. Phys, 154, 284

Press, W. H., Teukolsky, S. A., Vetterling, W. T., & Flannery, B. P., 1992 Numerical Recipes, 2nd ed., Cambridge University Press

Roe, P. L. 1986, Ann. Rev. Fluid Mech., 18, 337

Roe, P. L. 1981, J. Comput. Phys., 43, 357

Roe, P. L.& Balsara, D. S. 1996, SIAM J. Appl. Math., 56, 57

Ryu, D., & Jones, T. W. 1995, ApJ, 442, 228

Ryu, D., Jones, T. W., & Frank, A. 1995, ApJ, 452, 785

Ryu, D., Miniati, F., Jones, T. W., & Frank, A. 1998, ApJ, 509, 244

Shu, C. W. 1988, J. Comput. Phys., 77, 439

Shu, C. W.,& Osher, S. 1989, SIAM J. Sci. Comput., 83, 32

Sod, G. A. 1978, J. Comput. Phys., 27, 1

Sutherland, R. S., Bisset, D. K., & Bicknell, G. V. 2003, ApJS, 147, 187

Stone, J. M., & Norman, M. L. 1992, ApJS, 80, 791

Tóth, G. 2000, J. Comput. Phys., 161, 605

Tóth, G., & Roe, P. L. 2002, J. Comput. Phys., 180, 736

Toro, E. F., 1999 Riemann Solvers and Numerical Methods for Fluid Dynamics, 2nd ed.,
    Springer

Truelove, J. K., Klein, R. I., McKee, C. F., Holliman, J. H., II, Howell, L. H., Greenough,
    J. A., & Woods, D. T. 1998, ApJ, 495, 821

Van Leer, B. 1979, J. Comput. Phys., 32, 101.

Yirak, K., Frank, A., Cunningham, A., & Mitran, S. 2008, ApJ, 672, 996

Zachary, A. L., Malagoli, A., and Colella, P. 1994, SIAM J. Sci. Comput. 15, 2, 263

Ziegler, U. 2005a, Computer Physics Communications, 170, 153

Ziegler, U. 2005b, A&A, 435, 385